공학박사 학위논문

Sn particles produced by plasma-induced dewetting and its applications

플라즈마 디웨팅 법에 의한 Sn 분말 어레이 생성 및 그 응용에 관한 연구

2016 년 8 월

서울대학교 대학원

재료공학부

최 한 주

Sn particles produced by plasma-induced dewetting and its applications

지도 교수 이 정 중

이 논문을 공학박사 학위논문으로 제출함

2016 년 8 월

서울대학교 대학원

재료공학부

최 한 주

최한주의 공학박사 학위논문을 인준함

2016 년 8 월

위 원 장	황 농 문	(인)
부위원장	이 정 중	(인)
위 원	김 현 이	(인)
위 원	김 성 동	(인)
위 원	한 영 훈	(인)

Abstract

Metal film deposited on glass substrate by physical vapor deposition is energetically in a metastable state. When sufficient energy is applied, the film dewets into a set of particles by means of diffusion to minimize the total energy in the system. Metal film dewetting is initiated by hole formation, which is activated by either spinodal dewetting or hole nucleation and growth mechanism. Depending on the type of hole formation, the resulting particles vary in size and size distribution. Such observations have generally been used to distinguish the dominant mechanisms of the dewetting process.

In this work, the dewetting of Sn films was investigated. Behaviors of both spinodal dewetting and hole nucleation and growth were observed when 50 to 2000 nm thick Sn films were dewetted under ICP-generated H_2 plasma. At low film thicknesses, the dewetted particle diameter exhibited a spinodal-like behavior by varying exponentially to the film thickness with powers close to 5/3. At higher film thicknesses, a linear growth was observed in particle diameter with respect to film thickness, which implied that film dewetting was activated by hole nucleation and growth.

Several attempts were made to control the size and size distribution of the dewetted Sn particles. Input RF power was a dominant factor controlling the electron temperature and the density of plasma. When this parameter was increased, varying particle size and size distributions were observed at same film thickness. The capability of film dewetting was expanded when introducing repeated dewetting and templated substrates. Implementation of repeated dewetting resulted in higher particle density and bimodal particle distribution at appropriate first and

second film conditions. Also, templated substrates enabled the production of particles of similar size at desired locations.

The preliminary studies of Sn film dewetting were applied in two industrial applications. The first application was in the fabrication of solder bumps, which are interconnections built to transfer signals between a semiconductor chip and its external circuitry. The current solder bump process requires a lengthy procedure, which includes two sets of photolithography. The number of photolithography was reduced to one by utilizing the self-assembling nature of metal film dewetting.

Sn film dewetting was also applied in producing metal-based mesh-type transparent conductive film. The rapid and non-thermal characteristics of plasma-induced dewetting allowed a uniform distribution of Sn particles on polymer substrates. These particles were used as a mask layer to outline the mesh areas in the subsequent conductive layer. By controlling the size of the particle mask, conductive films with varying transmittance and resistance values were obtained.

The deposition of Sn films and other metal films were conducted by magnetron DC sputters. Plasma treatment of the Sn films was carried out in a separate vacuum chamber with an external ICP source installed. The surface morphologies of the dewetted particles and transparent conductive film samples were monitored by an ex-situ field emission scanning electron microscopy. The SEM images were analyzed using a computer software to perform a statistical analysis of dewetted particles.

Keywords: Dewetting, Plasma, Tin, Particle, Solder bump, Transparent conductive film, ICP

Student number: 2010-23199

Table of Contents

List of Tables

List of Figures

Figure 3-3-5. SEM images of Sn particles after repeated dewetting process. Thickness of first and second films as well as RF power of H_2 plasma treatment are indicated in each image.

Figure 3-3-6. SEM images of Sn film during repeated dewetting process. Times in each image refer to H_2 plasma treatment time of second film. t_1 and t_2 refer to the thickness of first and second films. Plasma treatments were conducted at RF 500 W and 300 W for t_1 and t_2, respectively.

Figure 3-3-7. SEM images of single and repeated dewetting process of Sn film. Corresponding histograms of the particle size distribution are shown next to the SEM images. Film thickness and plasma treatment power are indicated in each image.

Figure 3-3-8. Histograms of particle size distributions of single and repeated dewetting process of 300 nm and 300 nm/300 nm Sn films. H_2 plasma treatment was conducted at RF 500 W for 2 minutes.

Figure. 3-3-9. SEM images of Sn particles after single and repeated dewetting.

Figure 3-3-10. SEM images of templated substrates used in experiment.

Figure 3-3-11. SEM images of dewetted Sn particles on template A. Plasma treatment was conducted at RF 700 W for 30 minutes. Sn film thickness is indicated in each image.

Figure 3-3-12. SEM images of dewetted Sn particles on template B. Plasma treatment was conducted at RF 700 W for 30 minutes. Sn film thickness is indicated in each image.

Figure 3-3-13. SEM images of dewetted Sn particles on template C. Plasma treatment was conducted at RF 700 W for 30 minutes. Sn film thickness and trench width are indicated in figure.

Figure 3-5-5. SEM images of Au mesh film on PC substrates. H_2 plasma treatment time and open area percentage of Au mesh are indicated on top left and right corners of each image.

Figure 3-5-6. Transmittance of Au mesh film on PC substrate as a function of wavelength.

Figure 3-5-7. XPS data of polycarbonate substrate surface after H_2 plasma treatment. Plasma treatment time is indicated in each plot.

Figure 3-5-8. Normalized transmittance of polycarbonate substrate after H_2 plasma treatment.

I. Introduction

1.1 Plasma dewetting of metal film

Metal films deposited on glass substrate via sputtering or evaporation are energetically in a metastable state. Thus, when sufficient amount of energy is applied, a natural phenomenon called dewetting occurs by means of diffusion to minimize the total energy in the system (Figure 1-1-1) [1]. The energy balance in the film-substrate system is comprised of three interfacial energies: film-substrate, substrate-vacuum, and film-vacuum [2]. As shown in Figure 1-1-2, the equilibrium shape of the film on substrate surface is explained by Young's equation:

$$\gamma_{sub-vac} = \gamma_{film-sub} + \gamma_{film-vac} \cos\theta_c \quad (1)$$

where $\gamma_{sub\text{-}vac}$ is the substrate to vacuum interfacial energy, $\gamma_{film\text{-}sub}$ is the film to interfacial surface energy, $\gamma_{film\text{-}vac}$ is the film to vacuum interfacial energy, and θ_c is the contact angle of the film which is defined by the relative strengths of the interfacial energies. When $\gamma_{sub\text{-}vac}$ is larger than the sum of $\gamma_{film\text{-}sub}$ and $\gamma_{film\text{-}vac}$, the film is energetically stable and retains its flatness on the substrate surface. Conversely, if $\gamma_{sub\text{-}vac}$ is less than the sum of $\gamma_{film\text{-}sub}$ and $\gamma_{film\text{-}vac}$, the film is considered metastable (or unstable) and dewetting occurs to form the corresponding equilibrium contact angle.

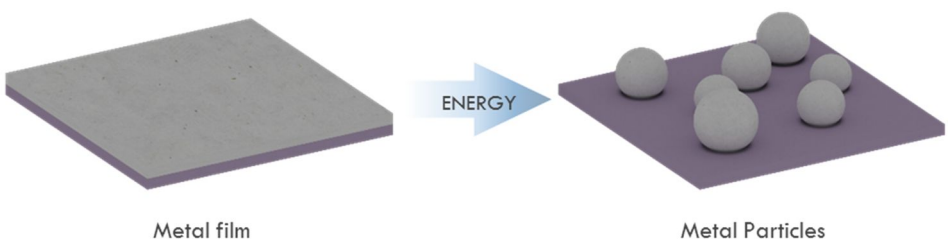

Figure 1-1-1. Schematic of metal film dewetting into metal particles at sufficient energy supply.

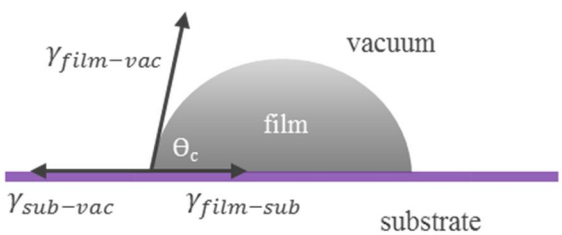

Figure 1-1-2. Equilibrium shape of film on substrate surface [2].

1.2 Hole formation mechanisms in metal film dewetting

Although the island morphology is preferred energetically to a flat film, a flat film is still metastable. Thus, a substrate-exposing hole formation step is necessary for the surface-energy-driven agglomeration to take place. There are two known mechanisms of hole formation in film dewetting. First, spinodal dewetting occurs when the film is in its liquid-state [3-6]. In thin films, thermal motion of particles in the film causes a certain roughness in the film. This roughness is often referred to as thermal fluctuation (Figure 1-2-1) [4]. There are several forces acting in the film, two in particular that oppose each other and influence this thermal fluctuation [3]. Van der Waals is a cohesive force within the film that intensifies the thin and thicker regions. Surface tension is an adhesive force between film and substrate and resists the strengthening of thermal fluctuation. When the magnitude of the van der Waals force is greater than that of the surface tension, thermal fluctuation is amplified, and the film ruptures with a spacing of specific wavelength.

The other hole formation mechanism is called hole nucleation and growth, and it is discussed in both liquid and solid states of the film [7-10]. This mechanism is primarily activated by film defects. In polycrystalline films, the grain boundaries are the site of film defects. A force balance equation in the grain boundary can be expressed as follows:

$$\gamma_{gb} = 2\gamma_f \sin\phi \tag{1}$$

$$\phi = \sin^{-1}\left(\gamma_{gb}/2\gamma_f\right) \tag{2}$$

where γ_{gb} is the grain boundary energy, γ_f is the film to vacuum interfacial energy, and φ is the groove angle, which defines the groove depth in the grain boundary by the relative strengths of the two energies (Figure 1-2-2) [7]. When φ is sufficiently high, the groove depth increases far enough to reach the surface of the substrate, and the grain boundary is subjected to hole formation. Given that grain boundaries have varying energies, hole formation mostly occurs at grain boundaries of high energies.

Depending on the type of hole formation activated, the resulting particles show different characteristics. For example, when a thin iron film was dewetted by pulsed laser irradiation, spinodal-like dewetting characteristics were observed, where particle spacing and particle diameter varied exponentially to the film thickness with powers of 2 and 5/3, respectively [11]. On the other hand, when Au and Cu films were dewetted by electron beam and Ar plasma through hole nucleation and growth, the particle diameter had a linear relationship with the film thickness [12, 13].

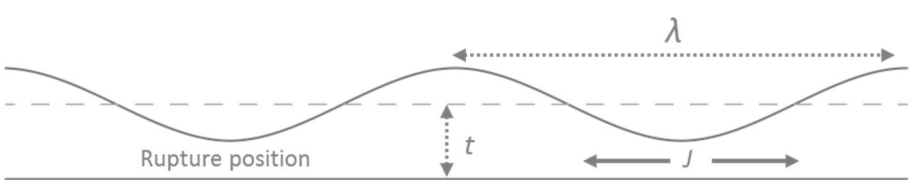

Figure 1-2-1. Schematic of thermal fluctuation in thin liquid film [4].

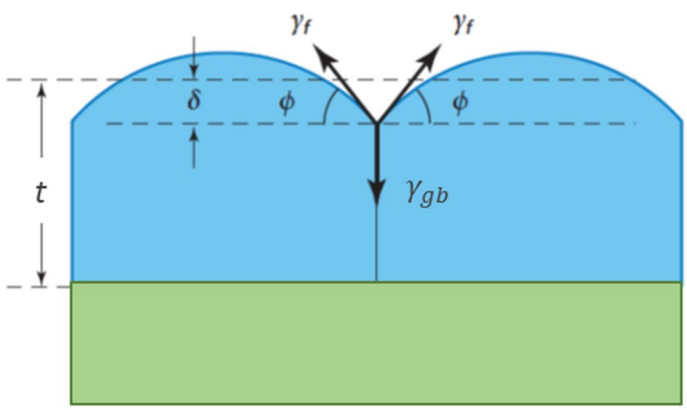

Figure 1-2-2. Schematic cross-section view of a two grain polycrystalline film [7].

1.3 Film dewetting model

A study conducted by Danielson et al. proposed a model to describe the stages involved in metal film dewetting (Figure 1-3-1) [1]. In this model, the dewetting proceeds in the following order:

a. Critical hole formation,

b. Hole edge thickening,

c. Hole edge breakdown,

d. Hole finger formation and growth, and

e. Island formation.

For surface-energy-driven dewetting to occur and proceed, a substrate-exposing hole of critical size must first be formed (step a). It is at this location where the dewetting of film begins.

Once the substrate is exposed and hole is produced, hole edge thickening causes mass to flow from film edge to the neighboring flat film, resulting in expansion of the hole area (step b). This hole expansion is further advanced by hole edge breakdown in which the accumulated mass at film edge begins to break into a set of high and low local curvatures due to Rayleight instability (step c). In step d, the high local edge curvatures drive the film mass to flow away from these regions, resulting in equally spaced finger growth. In step e, these fingers then break into discrete islands by a second Rayleigh instability.

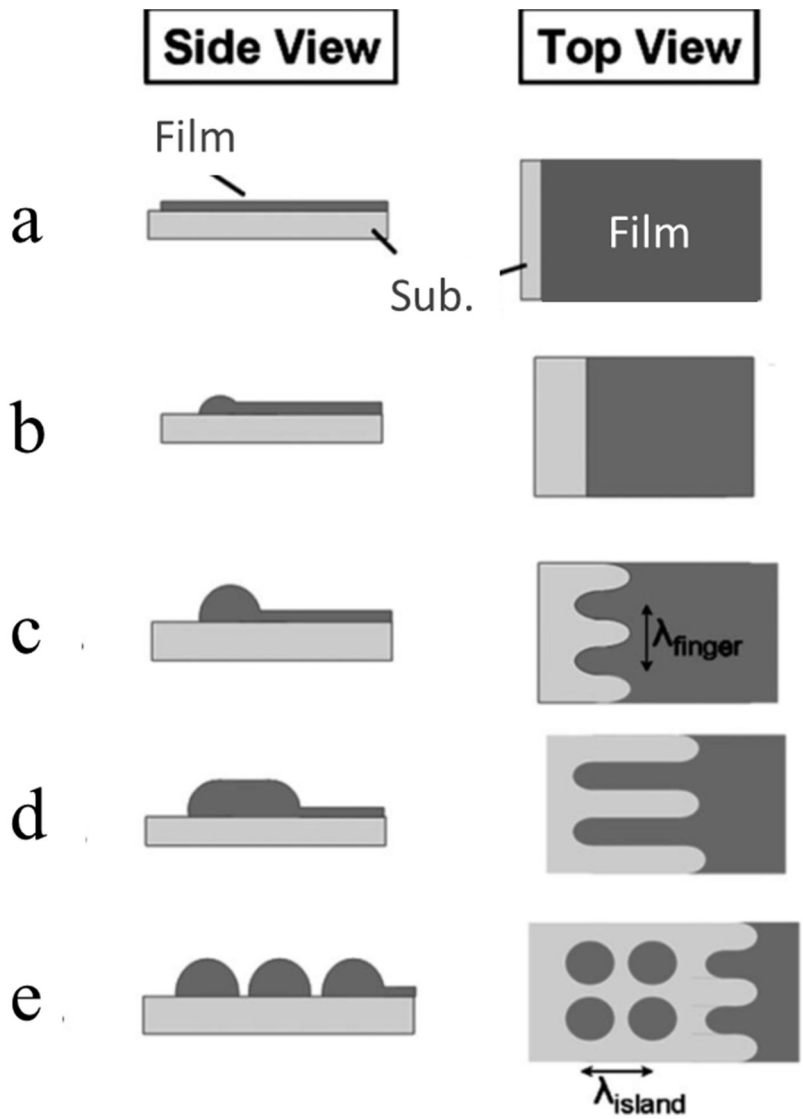

Figure 1-3-1. Illustration describing the five stages of metal film dewetting [1].

1.4 Applications of dewetted metal particles

Various research is conducted using the dewetting phenomenon of metal film. For example, when Au nanoparticles were incorporated by laser annealing in the PEDOT active layer during the synthesis of organic solar cells, the current density of the device improved by an increased number of photons in the active layer due to enhanced forward scattering [14]. For an antibacterial purpose, Au nanoparticles were formed by thermal annealing on TiO_2 nanotube arrays. When bacteria made contact with the TiO_2 surface, a localized surface plasmon resonance (LSPR) effect induced by the Au nanoparticles disturbed the electron transport in the bacteria's respiratory chain and caused the bacteria to exterminate [15]. For structural applications, research had been conducted to fabricate nanorodes in top-down or bottom-up direction by using the dewetted metal particles as an etch mask layer or a catalyst for epitaxial growth [16, 17].

In this research, the dewetting behaviors of low melting point metal were investigated by plasma treating Sn film ($T_m \approx 232\ ^oC$). Sn films were deposited by a DC magnetron sputter on SiO_2/Si substrates and were plasma treated under an H_2 environment using an inductively coupled plasma (ICP) source. A range of test conditions were evaluated to observe changes in particle size and size distribution. As an attempt to imitate the Sn solder bumps used in semiconductor packaging, Sn film dewetting was experimented on a templated substrate to produce an array of ordered Sn particles. Also, utilizing the rapid and non-thermal characteristics of the plasma treatment process, the study was applied to fabricate a meshed type metal transparent conductive film on polymer substrates.

II. Experimental

2.1 Deposition method

2.1.1 Substrates

Depending on the purpose of the experiment, substrate material and surface topography were varied.

2.1.1.1 Smooth substrate

Si wafers coated with 500 nm silicon oxide were used. The Si wafer was boron-doped p-type with (100) orientation, having a resistivity range from 1 to 30 Ω·cm.

2.1.1.2 Templated substrate

Templated substrates A, B, and C (Figure 2-1-1) were prepared on (100) Si wafers coated with a silicon nitride layer. Square and circular arrays were patterned on the silicon nitride layer using photolithography and CF_4-base reactive ion etching. Template C was placed in 30 % KOH solution at 80 ^{o}C for a specific duration to produce tapered side-walls and leveled floors. After the anisotropic wet etch, the silicon nitride layer was removed by an additional reactive ion etching.

2.1.1.3 Polymer substrate

Polycarbonate (PC) was used as the polymer substrate. The thickness of the PC substrates were 1 mm.

2.1.2 Deposition system

The schematic of the DC magnetron sputter and the deposition condition are shown in Figure 2-1-2 and Table 2-1. Prior to deposition, all substrates (except

PC) were cleaned in ultrasonic acetone and ethanol baths for 15 minutes consecutively; PC substrates were cleaned in ethanol baths only due to its reaction with acetone. Sn was sputter deposited onto the substrates with a deposition rate of 100 nm per minute from a 99.999 % pure target.

Table 2-1. Experimental conditions of Sn film deposition.

Process	Sn deposition
Tool	DC magnetron sputter
Base Pressure (Pa)	2.6×10^{-4}
Operating Pressure (Pa)	1.35
Gas (sccm)	Ar 20
Input Power (W)	DC 100
Target	Sn 99.999 %
Deposition Rate (nm/min)	100

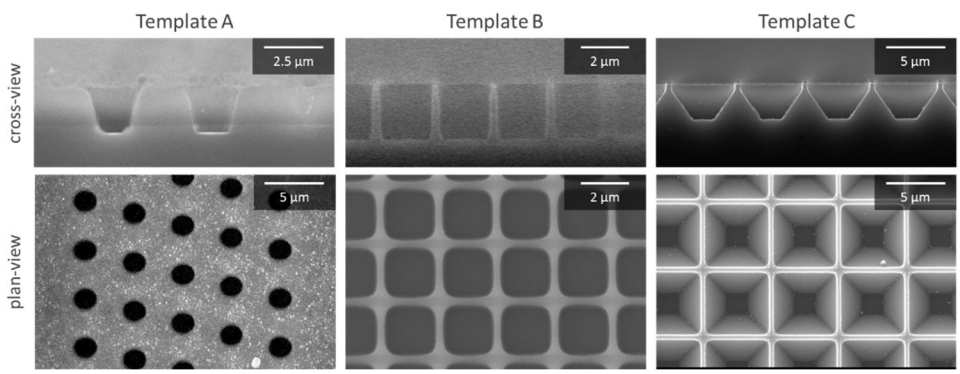

Figure 2-1-1. Templated substrates prepared on (100) Si wafers by photolithography and etch.

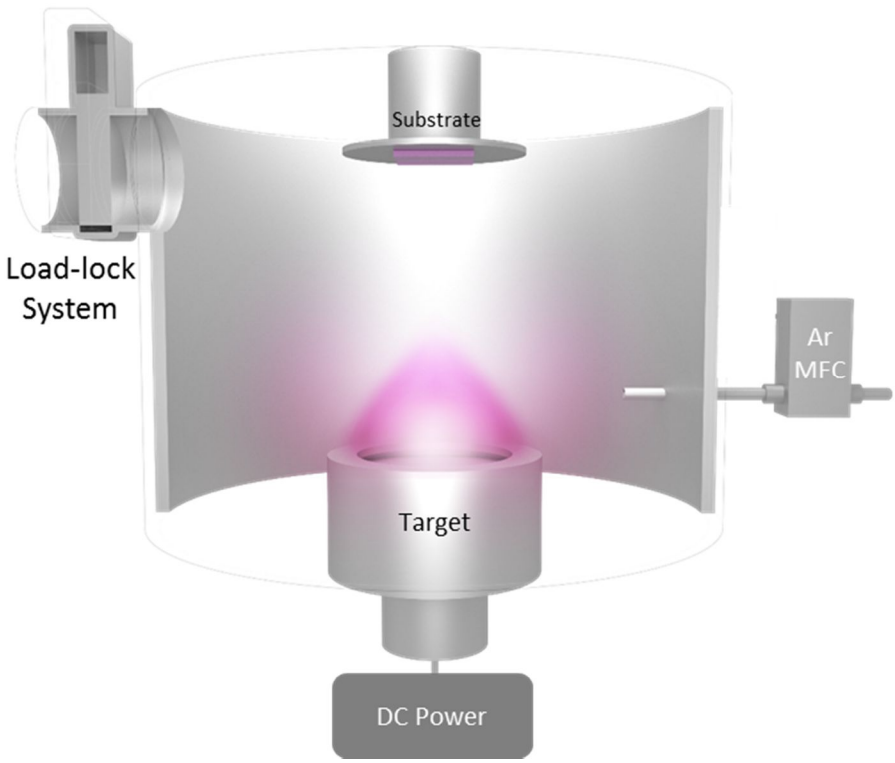

Figure 2-1-2. Schematic diagram of the DC magnetron sputter.

2.2 Plasma treatment method

The schematic of the ICP vacuum chamber and plasma treatment conditions are shown in Figure 2-2-1 and Table 2-2. Plasma dewetting was carried out at 2.7 Pa (20 mTorr) in an H_2 atmosphere. Plasma was generated by an external ICP source having a radio-frequency of 13.56 MHz. The RF power was induced through an Au-coated spiral Cu coil, which was installed above a quartz plate that served as the chamber lid. As a reference to the chamber user, the temperature of the substrate area was measured as a function of plasma treatment time (Figure 2-2-2).

Table 2-2. Experimental conditions of H_2 plasma treatment.

Process	H_2 plasma treatment
Tool	ICP vacuum chamber
Base Pressure (Pa)	6.7×10^{-5}
Operating Pressure (Pa)	2.7
Gas (sccm)	H_2 20 or Ar 20
Radio Frequency (MHz)	13.56
Input Power (W)	0, 300 – 400, 800

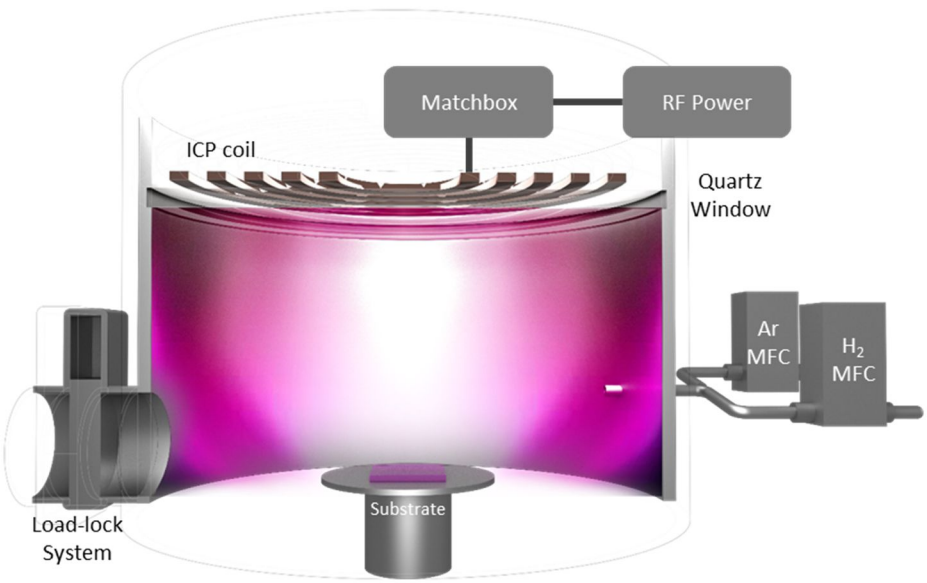

Figure 2-2-1. Schematic diagram of plasma treatment system.

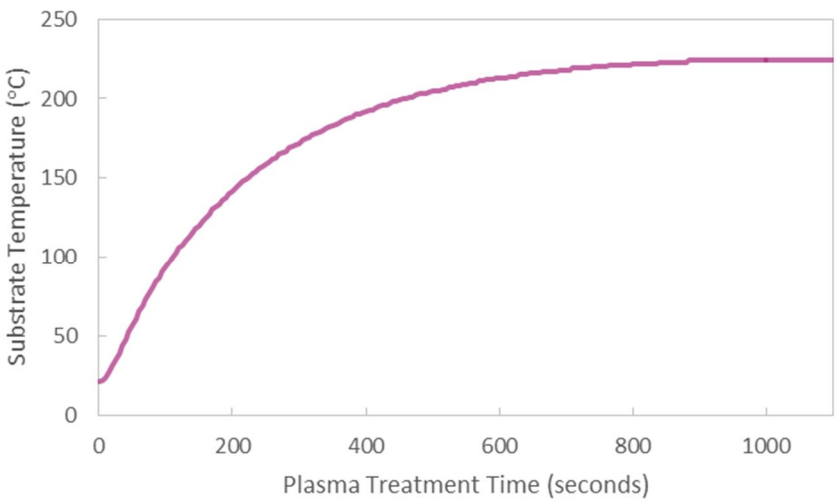

Figure 2-2-2. Substrate temperature of ICP chamber a function of plasma treatment time. The operating condition was 2.7 Pa with Ar flow of 20 sccm at 500 W input power.

2.3 Synthesis of metal mesh transparent conductive film

For one of the applications of Sn particles, the particles were used as a mask layer to produce the mesh areas in metal-based transparent conductive film (TCF). The following procedure was executed to synthesize the metal mesh TCF (Figure 2-3-1):

a. Deposition of Sn film on transparent (glass or PC) substrate,
b. Plasma treatment to dewet Sn film into particles,
c. Deposition of conductive film (Au, Ag, or Cu) over Sn particles, and
d. Removal of Sn particles by a selective wet etch using HCl solution.

2.3.1 Deposition of Au film

Au film was deposited by a DC magnetron sputter with a deposition rate of 6 nm per minute from a 99.99 % target.

2.3.2 Removal of Sn particles

During the last step of synthesizing metal mesh TCF, the samples were placed in ultrasonic hydrochloric acid solutions to remove the Sn particles. The molarity of the HCl solution and treatment time varied depending on the substrate material due to varying adhesion strength between film material and substrate surface. For Sn particles formed on glass substrates, the samples were treated in 0.05 M HCl for 4 hours. For PC substrate samples, the molarity and treatment times changed to 0.15 M and 2 hours.

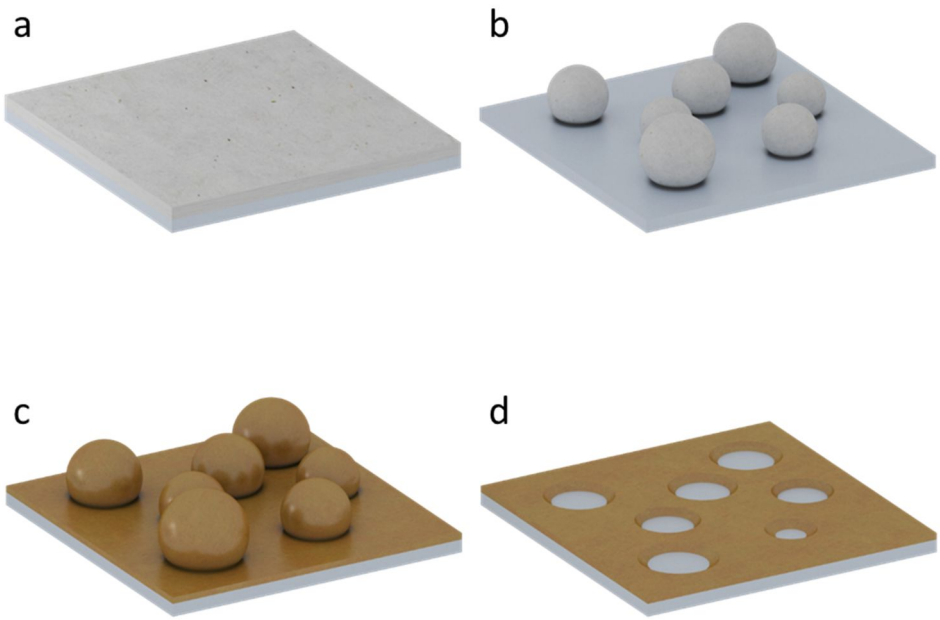

Figure 2-3-1. Process flow of metal-based transparent conductive film fabricated by plasma dewetted Sn particles.

2.4 Analysis method

2.4.1 Surface morphology inspection

The surface morphologies of the sample surface were inspected by field-emission scanning electron microscopy (FESEM, Hitachi SU70). The SEM images were analyzed using a computer software (Image-Pro Plus) to perform a statistical analysis of dewetted particles.

2.4.2 Film characterization

2.4.2.1 Crystal structure

Crystal structures of the Sn film and dewetted particles were analyzed by X-ray diffraction (XRD, Bruker. New D8 Advanced).

2.3.2.2 Optical transmittance

Optical spectra of metal mesh TCF samples were collected by a Varian Cary 5000 UV-Vis spectrometer in wavelengths ranging from 400 to 700 nm.

2.3.2.3 Binding energy

X-ray photoelectron spectroscopy of PC substrates were obtained by a Kratos Axis-His.

III. Results and discussion

3.1 Morphology evolution of Sn film dewetting

The morphology of Sn film was observed at different plasma treatment times (Figure 3-1-1). After depositing 1600 nm of Sn film on smooth SiO_2 substrate, plasma treatment was conducted from 0 to 300 seconds. The dewetting process began with hole formation (Figure 3-1-1b). With longer plasma exposure, the hole area expanded; progressively, the film developed into ridges (Figure 3-1-1f), which later detached into smaller islands, and the islands turned into sphere-forms, which are commonly referred to as particles. Unlike the dewetting model proposed by Danielson et al. in section 1.3, finger-like morphology was not monitored during the dewetting process of Sn film. The varying result seems to have come from the number of hole formation sites. In contrast to the dewetting model which proceeded from one hole (or film edge), the dewetting of Sn film began from simultaneous hole formations in multiple sites. Consequently, when the mass on film edge accumulated to the neighboring flat film area, the film agglomerated from multiple directions, producing the narrow ridges, which separated into discrete islands by Rayleigh instability.

Longer plasma treatment times were conducted to observe further changes in the particle morphology or particle size distribution. However, as shown in Figure 3-1-2, results of 10 minutes and 19 hours of plasma treatment conditions did not have any significant difference. Also, other treatment conditions, such as hydrogen gas thermal annealing and argon plasma treatment, were attempted to dewet the Sn films (Figure 3-1-3). Little or no change occurring on the Sn film

under these conditions suggested that sufficient energy transfer as well as oxide removal are both needed in dewetting the Sn films.

The morphological change of 200 nm Sn film was also inspected as shown in Figure 3-1-4. The dewetting sequence were very similar to that of 1600 nm Sn film except in the stage of hole formation. The holes in the thinner film appeared to be the cracks, which already existed in the as-deposited film, enlarged with plasma treatment. Figure 3-1-5 shows magnified images of the hole formation stage of 200 nm and 1600 nm Sn films for easier comparison.

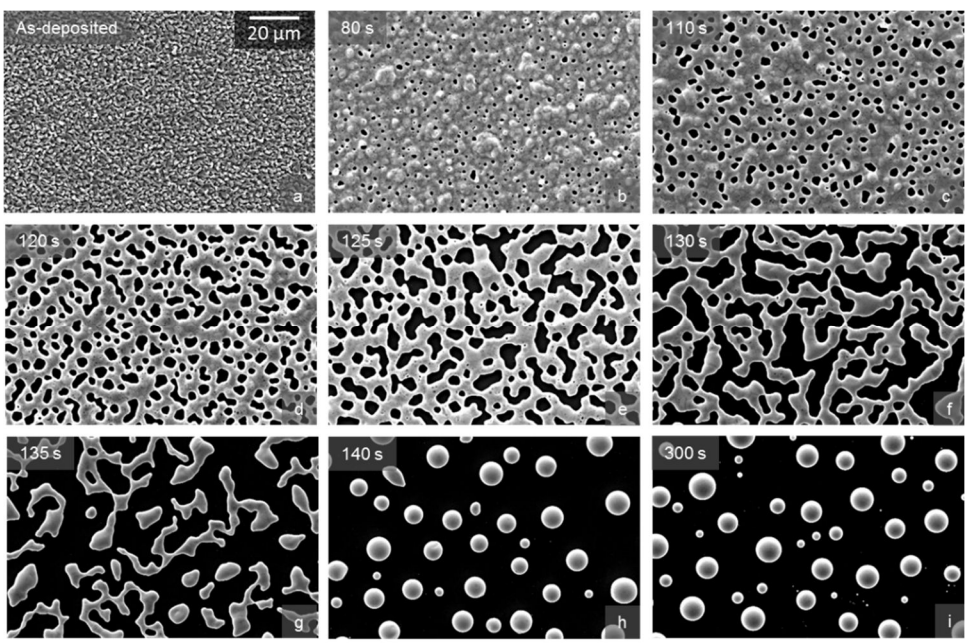

Figure 3-1-1. SEM images of 1600 nm thick Sn films after RF 300 W H_2 plasma treatment. Experiment times are indicated in each image.

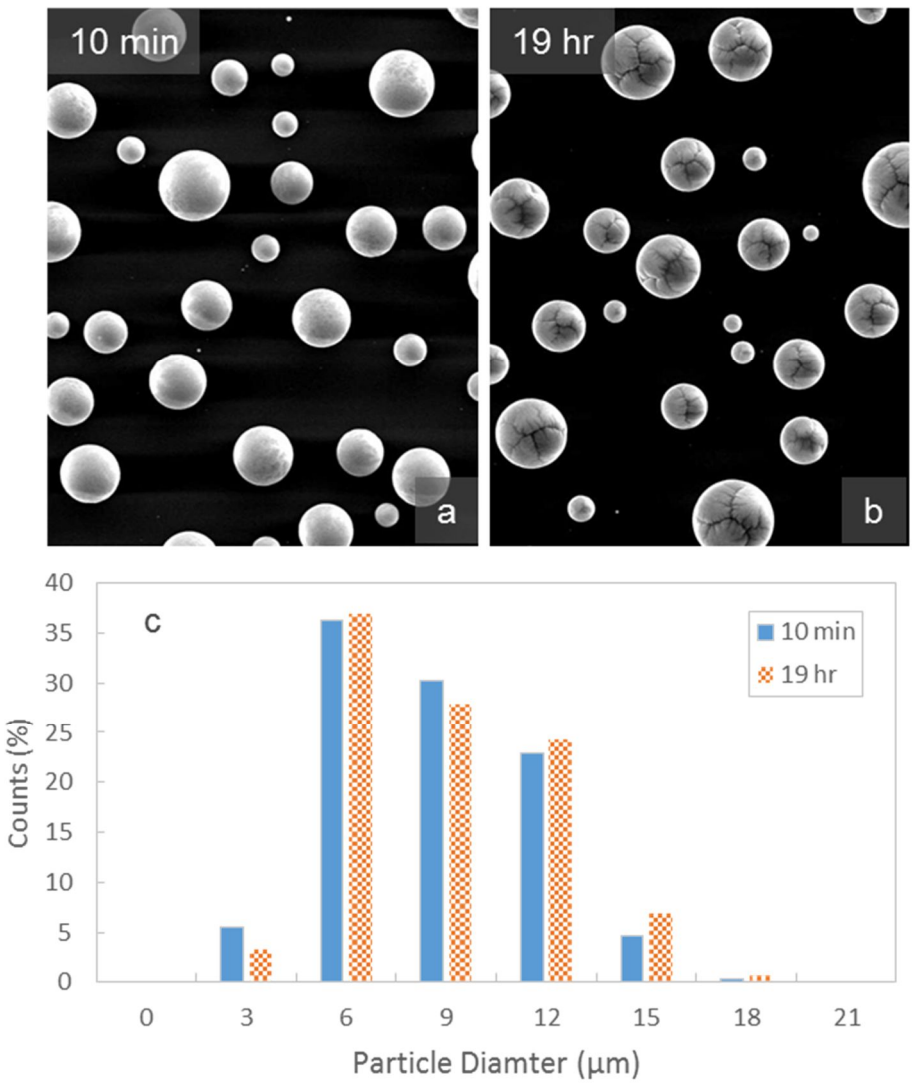

Figure 3-1-2. a, b) SEM images of 2000 nm thick Sn films after RF 400 W H_2 plasma treatment. Experiment times are indicated in each image. c) Histograms of particle size distribution produced from 2000 nm Sn films.

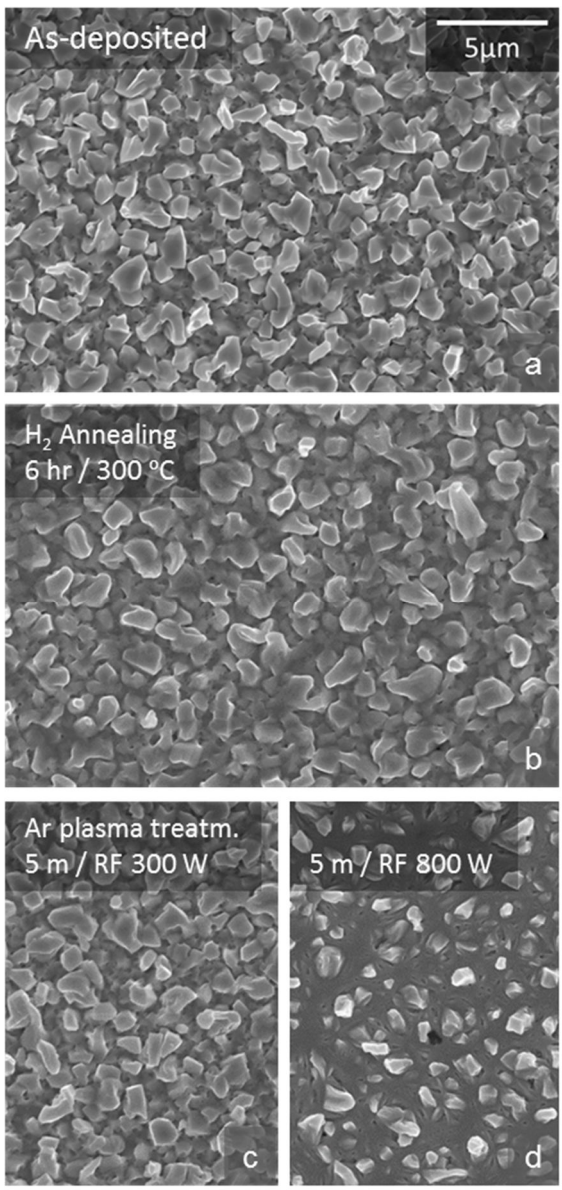

Figure 3-1-3. SEM images of 1600 nm thick Sn film after a) no treatment, b) 300 °C H_2 annealing for 6 hours, c) Ar plasma treatment at RF 300 W for 5 minutes, and d) Ar plasma treatment at RF 800 W for 5 minutes.

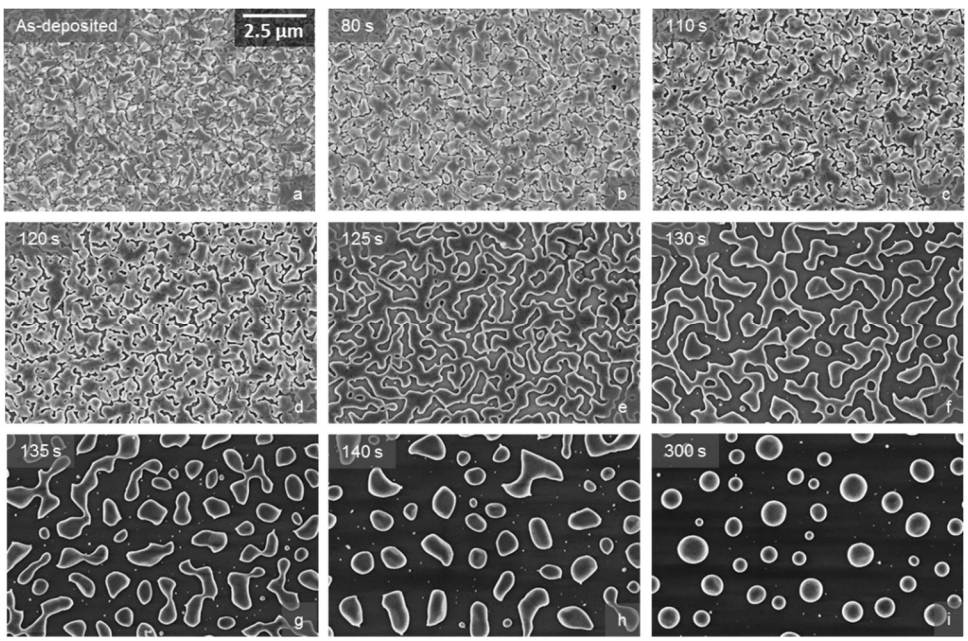

Figure 3-1-4. SEM images of 200 nm thick Sn films after RF 300 W H_2 plasma treatment. Experiment times are indicated in each image.

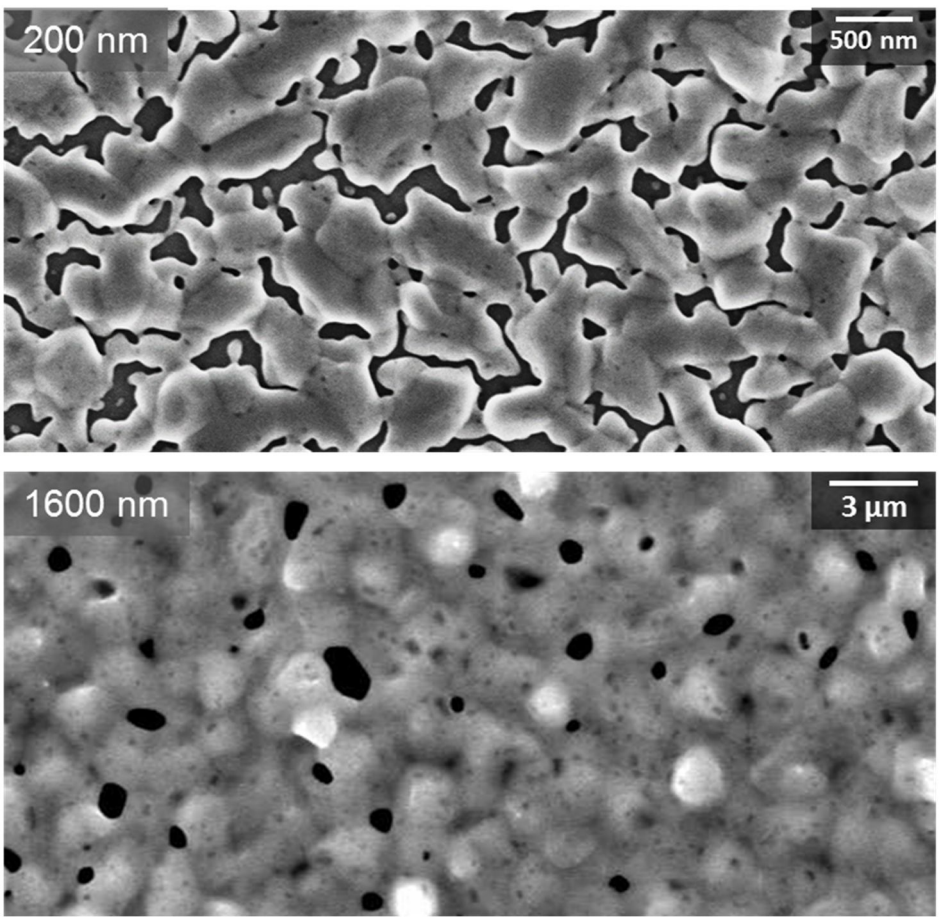

Figure 3-1-5. SEM images of Sn films at their hole formation stage. Initial film thickness is indicated in each image.

3.2 Dewetting mechanism of Sn film under hydrogen plasma treatment

Metal particles made from film dewetting are closely related to the thickness of their initial films. As it is described in the introduction, particle size varies with the 5/3 power of the film thickness in spinodal dewetting, while results of hole nucleation and growth show a linear relationship between particle size and film thickness [11-13]. Such observations have generally been used to distinguish the dominant mechanism of the dewetting process. In this experiment, behaviors of both spinodal dewetting and hole nucleation and growth were observed when the average diameter of Sn particles were plotted with respect to their initial film thickness as shown in Figure 3-2-1. The data in this figure were obtained by plasma treating Sn films from 50 nm to 2000 nm deposited on smooth SiO_2/Si substrates. Hydrogen plasma was used in the experiment to prevent oxidation and promote self-diffusion of the metal atoms. SEM images of each sample were analyzed using a computer software to collect statistical information of the particle diameters (Figure 3-2-2).

When drawing a best fit line through the data points from film thickness of 50 nm to 600 nm, the particle diameter varied exponentially to the film thickness with powers close to 5/3. On the other hand, particles produced from films above 600 nm to 2 μm showed a linear growth in particle diameter with respect to film thickness. Considering the low melting point of Sn film, it can be expected that the dewetting of thinner films were initiated in liquid-state, thus showing spinodal-like behavior.

Additional evidence of hole nucleation and growth behavior at thicker Sn films is shown in Figure 3-2-3. When conducting electron backscatter diffraction on a 1600 nm thick Sn film, nucleated holes were spotted in areas between grain boundaries. The different dewetting behaviors observed in the Sn films can be explained by discussing i) the energy gradient, and ii) gravitational force in the film. During plasma treatment, plasma energy is transferred to the film by accelerated ions bombarding the film surface. Inevitably, an energy gradient develops, and the atoms near the surface become more energetically active than the atoms in the bulk. At low film thickness, the energy difference between the surface and bulk is small. Thus, when sufficient plasma energy is applied, the film fluctuates or melts as a whole, causing spinodal dewetting. At higher film thicknesses, the energy difference between the surface and bulk atoms becomes more apparent. In these situations, the surface atoms diffuse and activate the dewetting process by means of hole nucleation and growth before sufficient plasma energy reaches the bulk.

In addition to the van der Waals force and surface tension mentioned in section 1.2, there is a third force that affects the activation of spinodal dewetting. This force is the gravitation force in film, which increases with the square of film thickness. When the film is thin, the gravitational force is small enough to be neglected. However, above a certain film thickness, the strength of the gravitational force becomes significantly large that it opposes the amplification of the thermal fluctuation [12].

According to Krishna et al, a thickness-dependent free energy curve is produced by considering the van der Waals force, surface tension, and gravitational

force in a metal film (Figure 3-2-4) [12]. In this curve, there are three distinct stability regimes: unstable, metastable, and stable. For typical metal films, the unstable regime and metastable regime lies before and after 1000 nm. When the film is thin and unstable, hole formation occurs through spinodal dewetting, whereas for films in the metastable regime, dewetting is initiated by hole nucleation and growth. In this experiment, where sputter deposited Sn film was treated with hydrogen plasma, the transition in dewetting behavior was observed at 600 nm, which is considered to be in close range to the transition thickness predicted by Krishna.

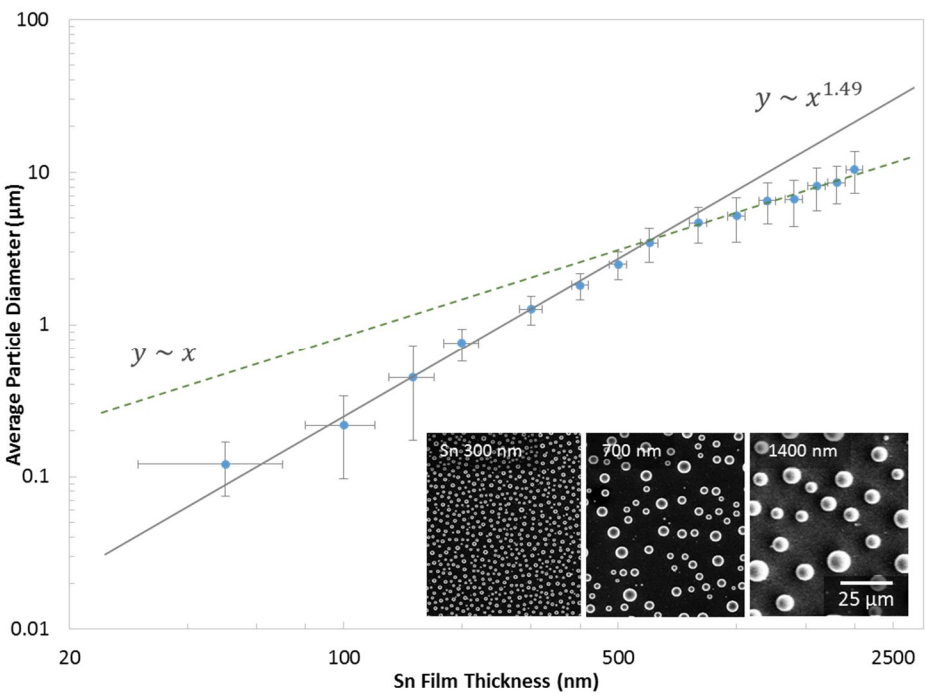

Figure 3-2-1. Average particle diameter as a function of initial film thickness of dewetted Sn films.

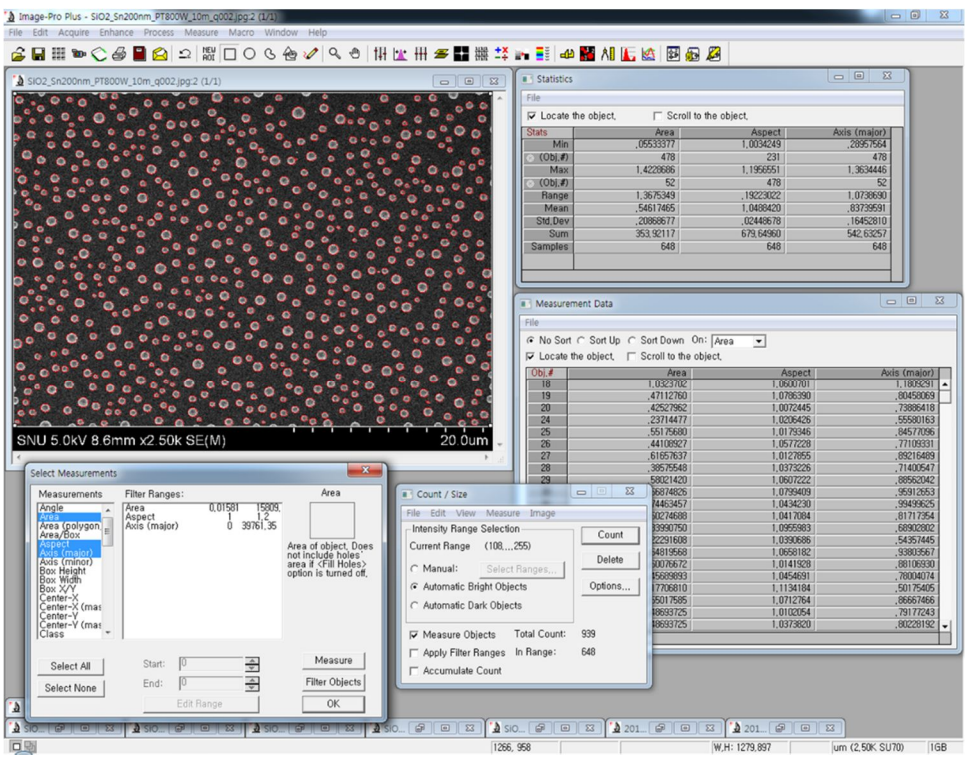

Figure 3-2-2. Snapshot of Image-Pro Plus, software used to collect statistical data of dewetted particles.

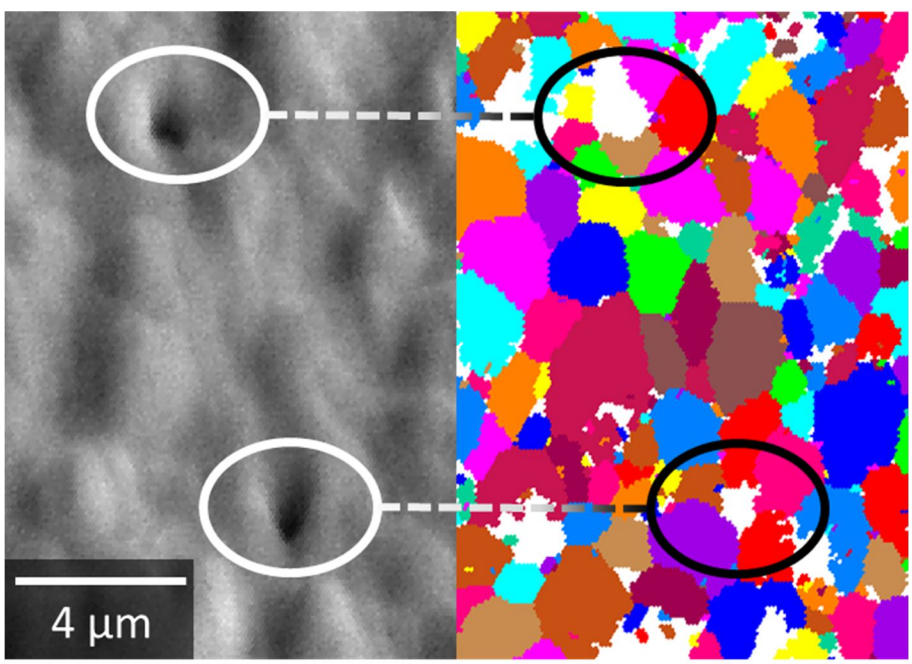

Figure 3-2-3. SEM (left) and EBSD (right) images of 1600 nm Sn film at hole formation stage.

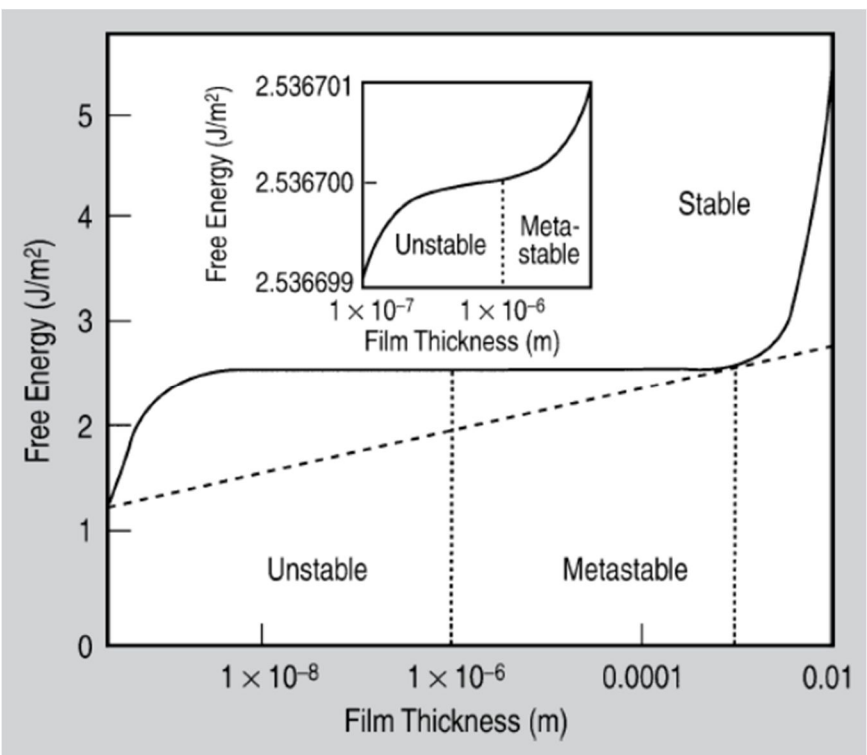

Figure 3-2-4. Free energy curve of a typical metal film [11].

3.3 Dewetted particle size and size distribution control

3.3.1 RF power effect

Same Sn films of 50 nm to 2000 nm were plasma treated at different RF powers as shown in Figure 3-3-1. At film thickness below 600 nm, an increase in particle size was observed at each film thickness when increasing the RF power. As the exponent values of the film thickness were increased closer to 5/3, it seemed that the tendency for spinodal-like behavior grew stronger. Similar results were observed when plotting the inter-particle distance of the dewetted Sn particles at the same film thickness regions (Figure 3-3-2). At film thickness above 600 nm, the results were contrary; the particle size decreased with increasing RF power.

RF power is a dominant factor controlling the electron temperature and the density of plasma. During plasma treatment, plasma energy is transferred to the film surface by ions which carry more or less uniform energy equivalent to the sheath potential. The density of these ions and sheath potential are determined by the plasma density and electron temperature, which both increase with increasing RF power [18].

A clear difference in particle size distribution was observed while comparing the results conducted at 300 W and 400 W of same film thickness. As shown in Figure 3-3-3, the range of the particle size distribution is narrower at the higher RF power. This change in particle size and size distribution is more apparent when the data is plotted as line graphs (Figure 3-3-4). When the RF power was increased, particle size and size distribution decreased while the number of particles per area steadily increased.

According to previous studies, when sufficiently high plasma energy was applied to dewet metal films through hole nucleation and growth, the ion bombardment energy was calculated to be higher than the minimum displacement threshold energy of the metal film but insufficient to sputter the metal atoms [19]. Increasing the RF power is presumed to cause more rapid diffusion of surface atoms and enhance the rate of hole nucleation. Subsequently, larger number of holes separate the film into smaller areas, which develop into thinner ridges that break up into particles of reduced size.

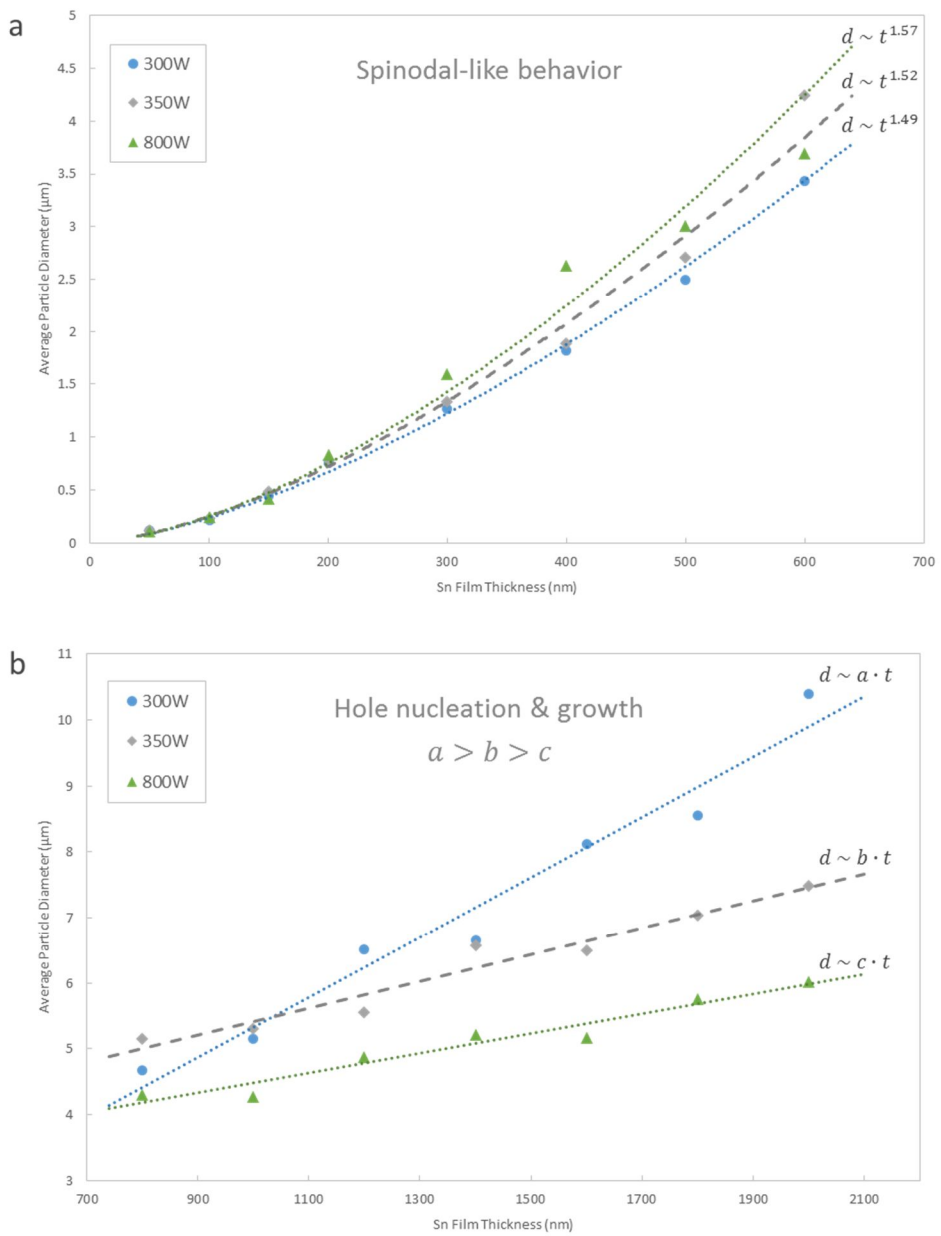

Figure 3-3-1. Average particle diameter as a function of initial Sn film thickness treated at various RF powers.

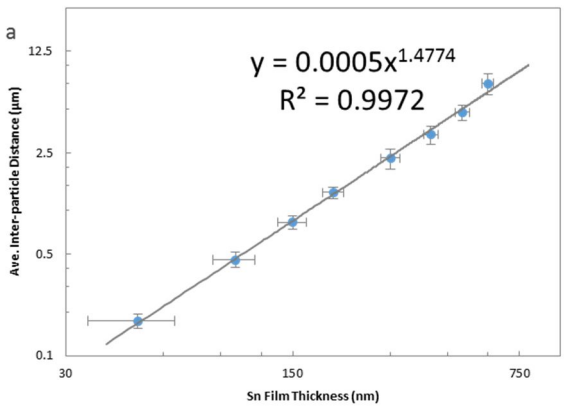
a
y = 0.0005x^1.4774
R² = 0.9972
Ave. Inter-particle Distance (µm)
12.5
2.5
0.5
0.1
30
150
750
Sn Film Thickness (nm)

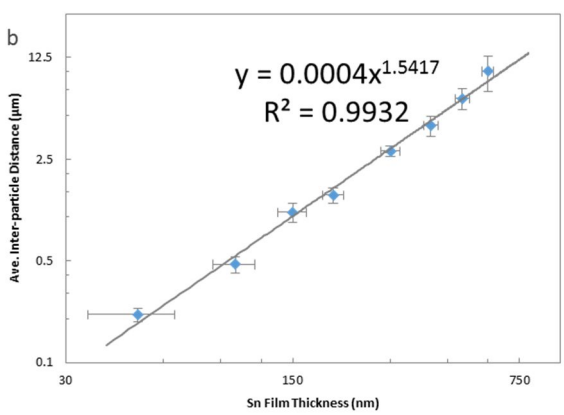
b
y = 0.0004x^1.5417
R² = 0.9932
Ave. Inter-particle Distance (µm)
12.5
2.5
0.5
0.1
30
150
750
Sn Film Thickness (nm)

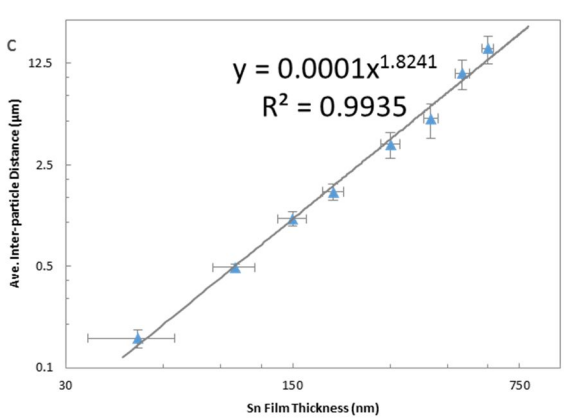
c
y = 0.0001x^1.8241
R² = 0.9935
Ave. Inter-particle Distance (µm)
12.5
2.5
0.5
0.1
30
150
750
Sn Film Thickness (nm)

Figure 3-3-2. Inter-particle distance of dewetted Sn particles as a function of Sn film. H_2 plasma treatment was conducted at a) RF 300 W, b) RF 350 W, and c) RF 800 W.

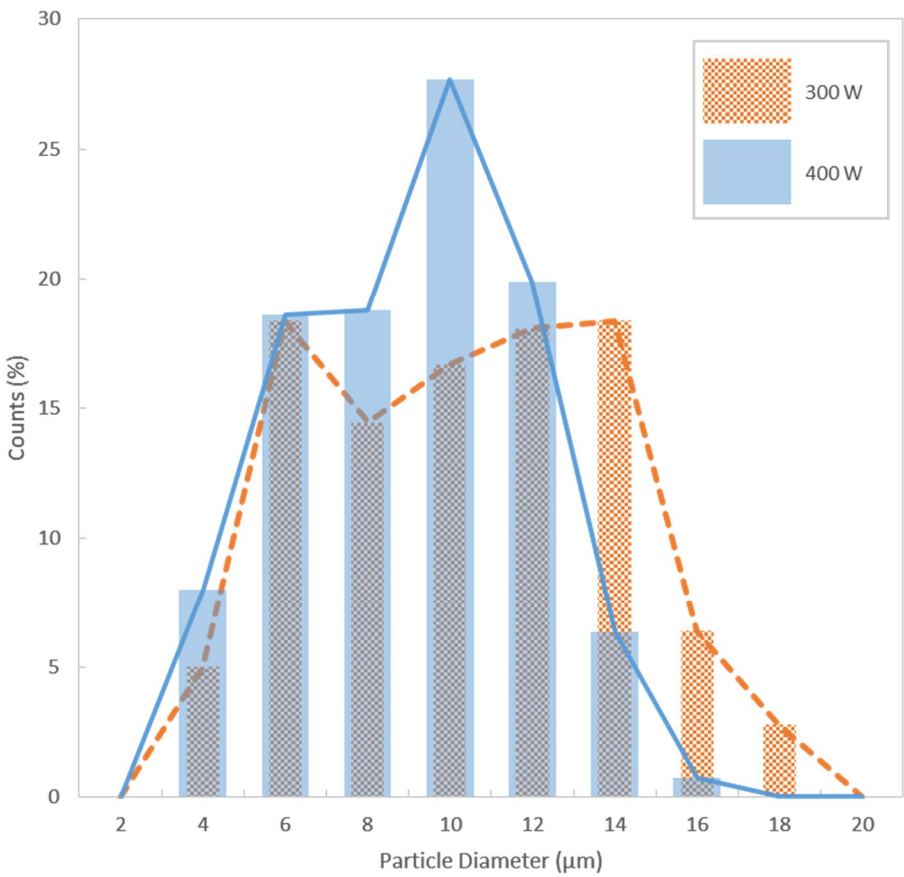

Figure 3-3-3. Histograms of particle size distributions produced by dewetting 1600 nm thick Sn films on smooth SiO_2/Si substrates at RF 300 W and 400 W.

a

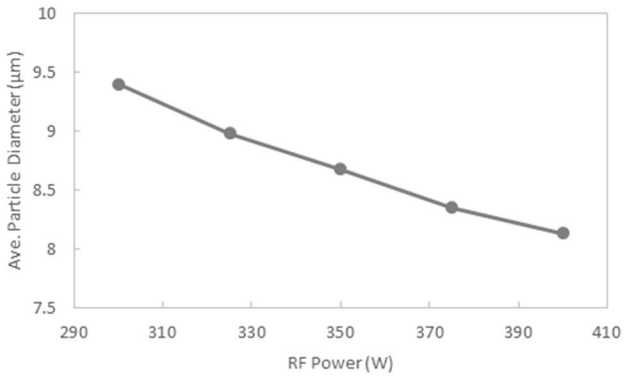
10
9.5
9
8.5
8
7.5
Ave. Particle Diameter (µm)
290
310
330
350
370
390
410
RF Power (W)

b

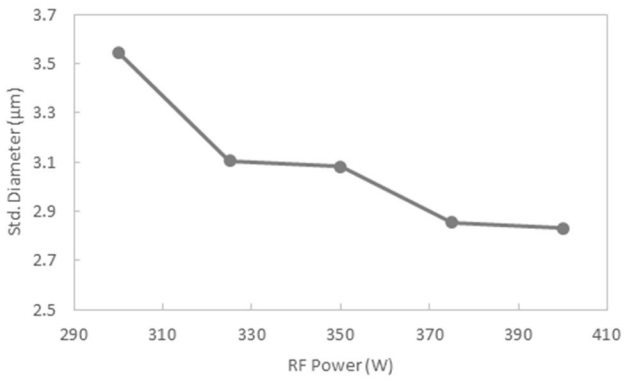
3.7
3.5
3.3
3.1
2.9
2.7
2.5
Std. Diameter (µm)
290
310
330
350
370
390
410
RF Power (W)

c

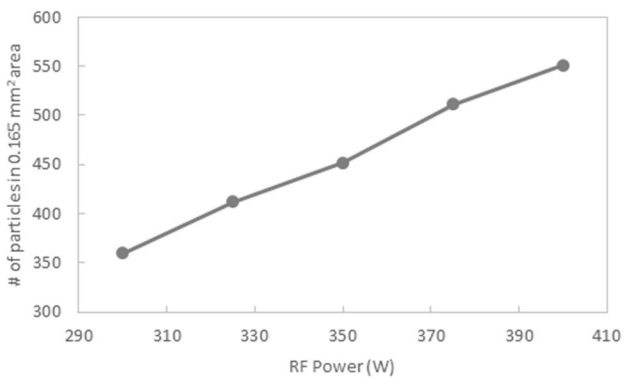
600
550
500
450
400
350
300
# of particles in 0.165 mm² area
290
310
330
350
370
390
410
RF Power (W)

Figure 3-3-4. a) Average particle diameter, b) standard deviation of the particle diameters, and c) number of particles per area as a function of RF power.

3.3.2 Repeated dewetting

In an attempt to produce other types of distributions, the dewetting process was conducted repeatedly: deposition and plasma treatment followed by a second set of deposition and plasma treatment. In repeated dewetting, results of the particle size and size distribution varied depending on the thickness of first and second Sn films. As shown in Figure 3-3-5, which denotes the thicknesses of the first and second films as t_1 and t_2, respectively, a bimodal distribution of particle size was produced when t_1 was greater than t_2. On the other hand, when t_1 was smaller than t_2, the resulting particle size and size distribution were similar to those of a single dewetting process of film thickness that is equivalent to the sum of t_1 and t_2.

To understand such results, the morphological change of the repeated dewetting process was explored. As shown in Figure 3-3-6, proceedings of the dewetting process of the second film was observed at varying plasma treatment times. When t_1 was greater than t_2, the particles of t_1 maintained their presence throughout the dewetting process. A small increase in the particle size was present due to the portion of the second film that was deposited on top and around. It appeared that the remaining portion of the second film dewetted with little influence of the initially dewetted particles. On the other hand, when t_1 was smaller than t_2, the presence of the t_1 particles disappeared during the dewetting of the second film. Since the relative size of t_1 particle was small compared to t_2, after

hole formation in the second film, the volume of t_1 particles merged with the volume of t_2, and dewetting proceeded as if a single layer film were being dewetted.

The histograms of the dewetted particles of single dewetting and repeated dewetting were placed together for comparison (Figure 3-3-7). The single dewetting results of 200 nm and 300 nm Sn films were compared with the result of 300 nm/200 nm repeated dewetting. Although the input RF powers of the plasma treatment conditions were not consistent, the particle size distribution of the repeated dewetting process seemed to have the sum of the two single dewetted particle size distributions. It is recommended this experiment be repeated with same RF power to verify the accuracy of this observation.

Repeated dewetting of same film thickness (300 nm/300 nm) was also conducted (Figure 3-3-8). Compared to the particle size distribution of a single dewetting, the size of the particles were in similar range, but the numbers of particles in each bin of the histogram nearly doubled. Figure 3-3-9 shows the particles dewetted from 600 nm film, and the contrast between the results of repeated and single dewetting are again observed.

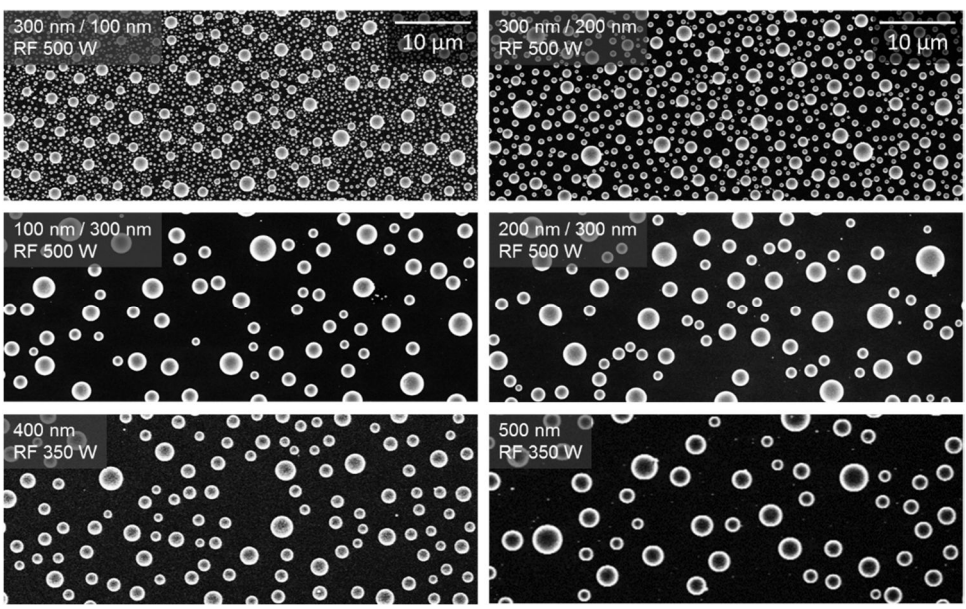

Figure 3-3-5. SEM images of Sn particles after repeated dewetting process. Thickness of first and second films as well as RF power of H_2 plasma treatment are indicated in each image.

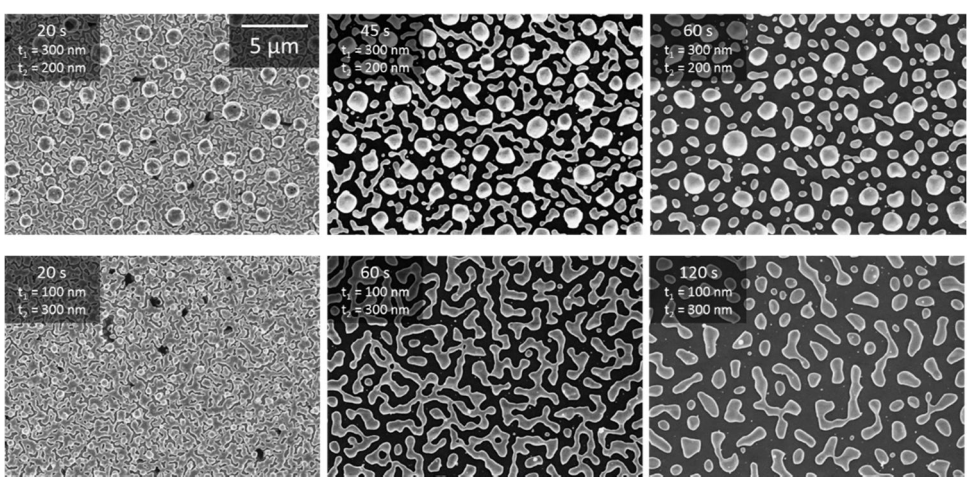

Figure 3-3-6. SEM images of Sn film during repeated dewetting process. Times in each image refer to H_2 plasma treatment time of second film. t_1 and t_2 refer to the thickness of first and second films. Plasma treatments were conducted at RF 500 W and 300 W for t_1 and t_2, respectively.

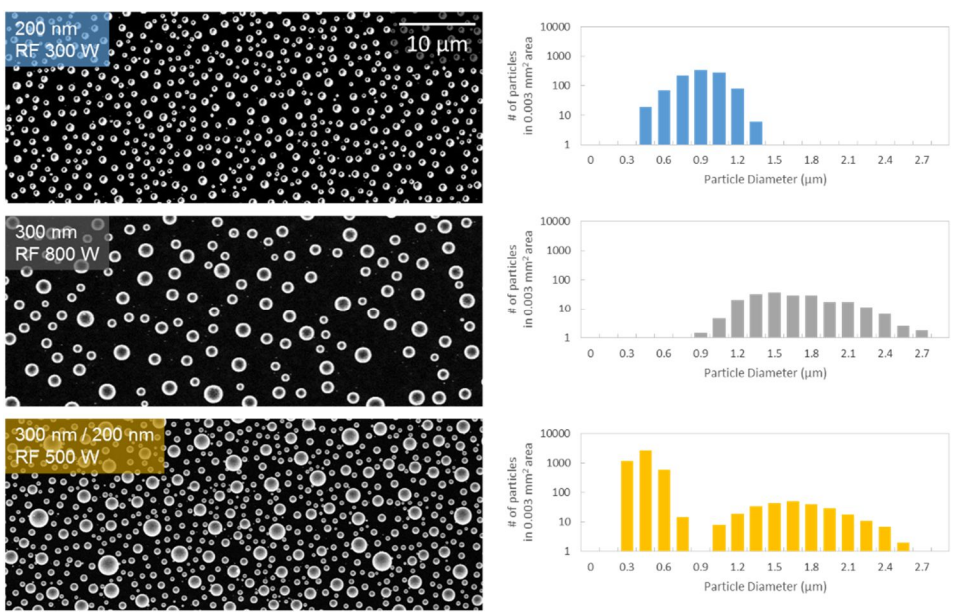

Figure 3-3-7. SEM images of single and repeated dewetting process of Sn film. Corresponding histograms of the particle size distribution are shown next to the SEM images. Film thickness and plasma treatment power are indicated in each image.

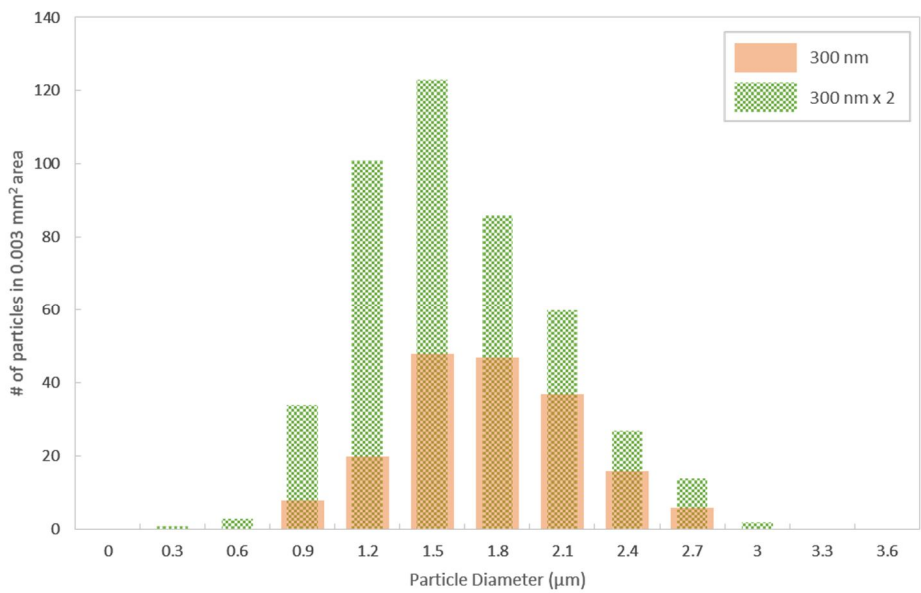

Figure 3-3-8. Histograms of particle size distributions of single and repeated dewetting process of 300 nm and 300 nm/300 nm Sn films. H_2 plasma treatment was conducted at RF 500 W for 2 minutes.

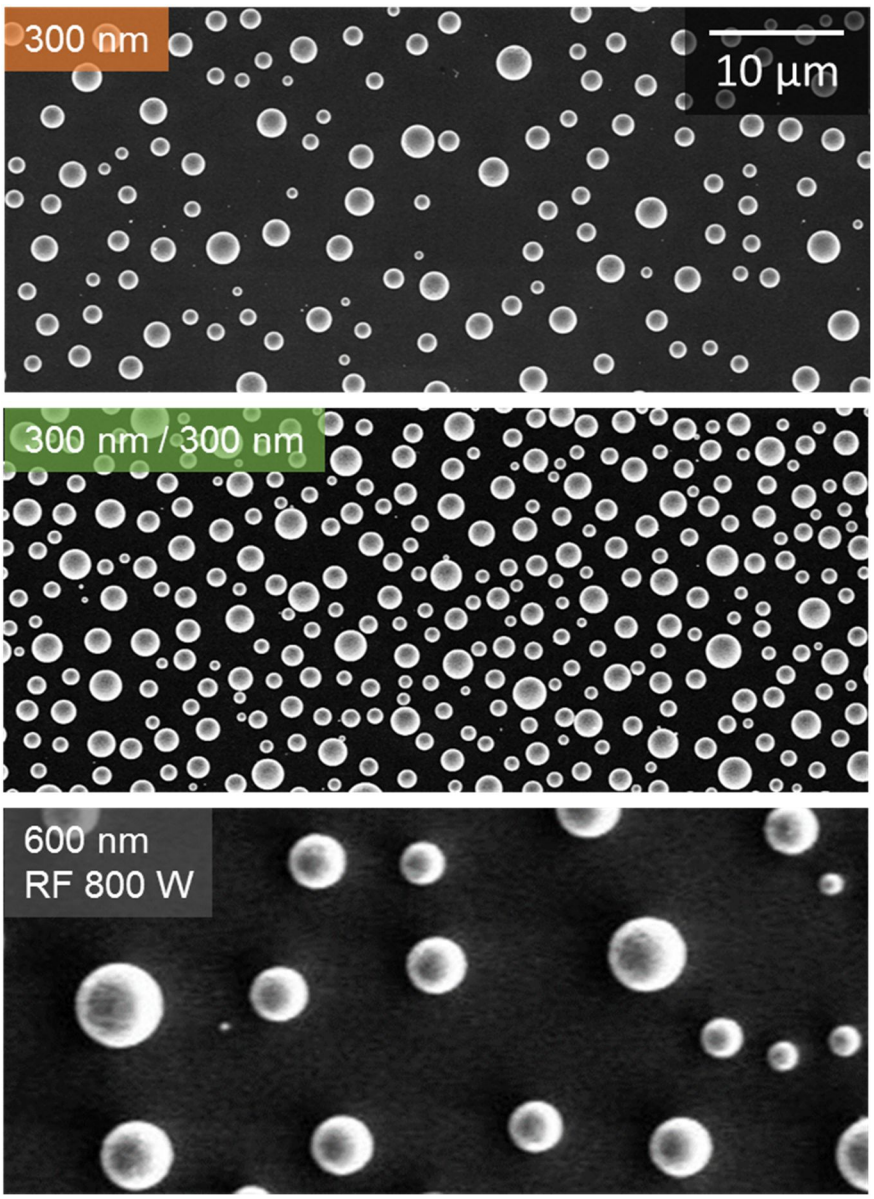

Figure. 3-3-9. SEM images of Sn particles after single and repeated dewetting.

3.3.3 Templated substrate

The dewetting phenomenon of Sn film under plasma treatment was also examined by varying the substrate template (Figure 3-3-10). The templated substrates were prepared by conducting a set of photolithography and etch at the Inter-university Semiconductor Research Center of Seoul National University.

3.3.3.1 Templates A & B

Plasma treatment results of Sn film on templates A and B are shown in Figure 3-3-11 and 3-3-12, respectively. Film thickness was varied from a few hundred nanometers to about 2 μm. Dewetted particles were observed both inside and outside the trench areas. At low film thickness, 3 to 5 discrete particles were formed inside the trench areas, and the number decreased at higher thicknesses. On template A, one particle of similar size was formed in each trench at 600 nm and above. While the particles located outside the trench continued to increase in size, the particles inside the trench area ceased to grow after 600 nm. Likewise, on template B, the particles formed on mesas, between the trenches, grew continuously with film thickness, whereas the particles formed on the trench interior walls maintained their size after 1 μm. In these templates, the particles formed outside the trenches were always larger than the particles formed inside.

3.3.3.2 Template C

The dewetting results of template C are shown in Figure 3-3-13. Compared to templates A and B, the major difference in template C was the tapered profile of

the trench sidewalls. Plasma dewetting of Sn film from 1500 nm to 4000 nm was conducted on trenches of varying widths from 5 μm to 20 μm. Unlike the results observed in templates A and B, all the particles were formed inside the trench interior.

To understand the contrasting results of template C from templates A and B, cross-SEM images before plasma treatment were observed as shown in Figure 3-3-14. Due to the trench sidewall profiles that were almost perpendicular in templates A and B, the thickness of the Sn film was not conformal. As oppose to the film deposited outside or on the mesas, thinner layers of Sn film were deposited on the trench interior. It is presumed that hole formations occurred at the trench corners or sidewalls where the film thickness was relatively thin. Since the deposited Sn film was thicker on the outside, the particles formed outside the trenches were larger at all film conditions.

On the other hand, the tapered sidewall profile enabled a more conformal film deposition on template C. Almost equal thicknesses of Sn film were deposited on every surface. Also, the sidewalls in template C were intentionally designed very narrow to have all the film mass fall into the trench areas.

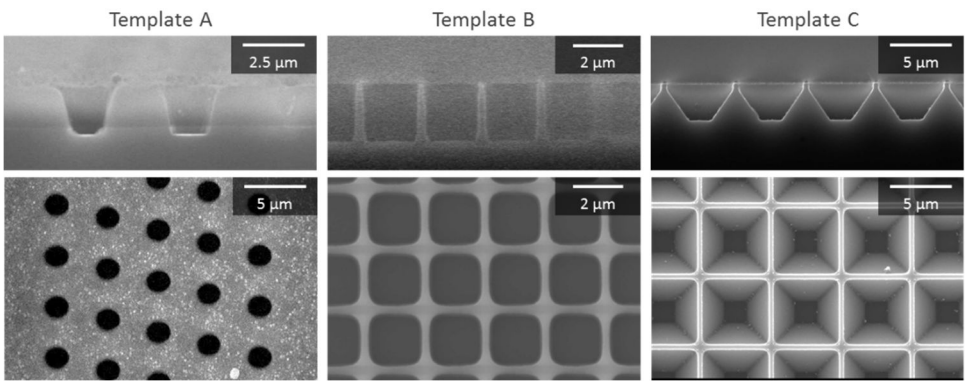

Figure 3-3-10. SEM images of templated substrates used in experiment.

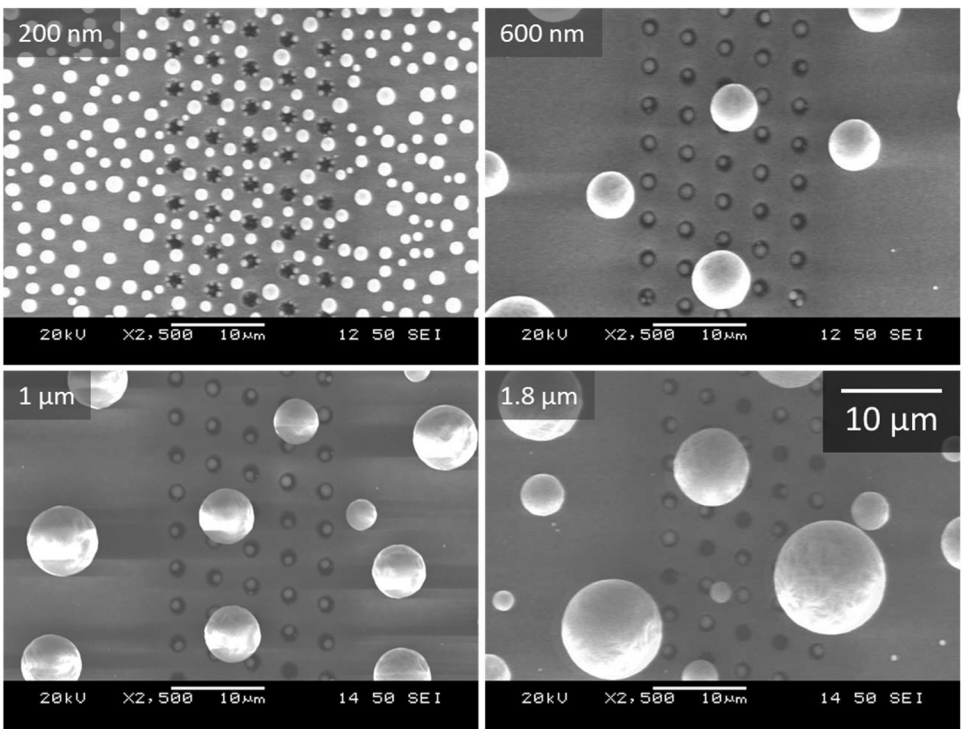

Figure 3-3-11. SEM images of dewetted Sn particles on template A. Plasma treatment was conducted at RF 700 W for 30 minutes. Sn film thickness is indicated in each image.

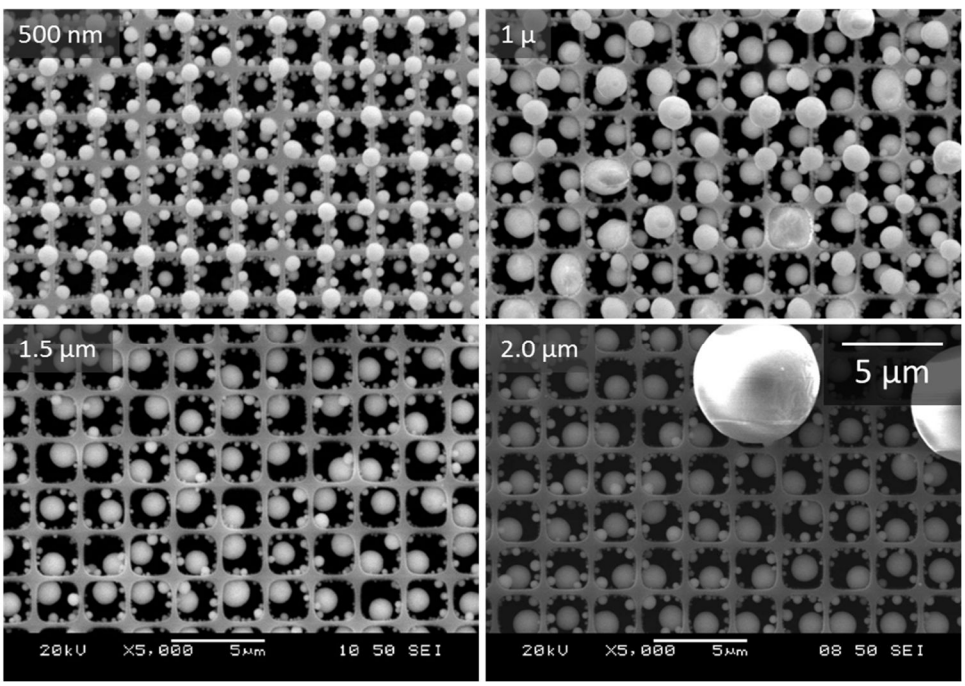

Figure 3-3-12. SEM images of dewetted Sn particles on template B. Plasma treatment was conducted at RF 700 W for 30 minutes. Sn film thickness is indicated in each image.

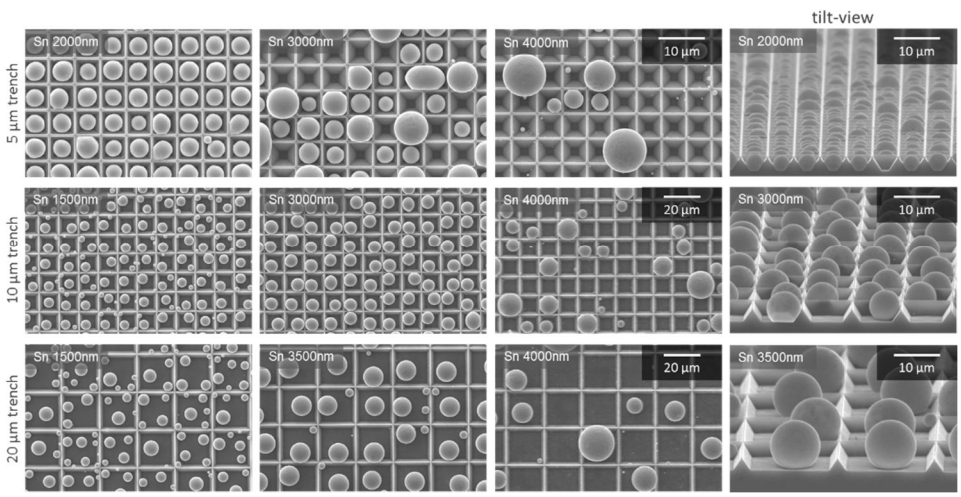

Figure 3-3-13. SEM images of dewetted Sn particles on template C. Plasma treatment was conducted at RF 700 W for 30 minutes. Sn film thickness and trench width are indicated in figure.

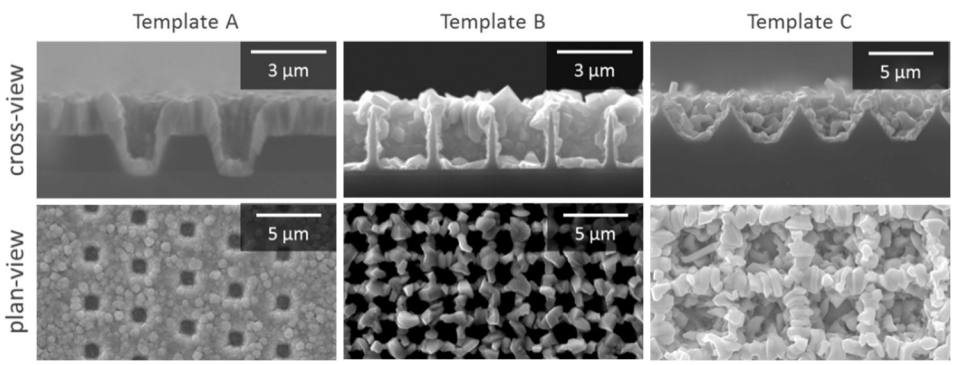

Figure 3-3-14. SEM images of Sn film on templates A, B, and C before plasma treatment.

3.4 Application I: Sn film dewetting for solder bump fabrication

3.4.1 Introduction of solder bump interconnections

Sn is a base material used for the fabrication of solder bumps (or solder joints), which are interconnections used in chip packaging to join a completed semiconductor chip to its external circuitry (Figure 3-4-1) [20]. Solder bumps are deposited on the metal pads of the semiconductor chip. In the conventional solder bump process, multi-step photolithography is performed twice: once to define the metal pad areas and another to outline the size and position of the solder bumps (Figure 3-4-2). Photolithography is very reliable and produces consistent results, yet the technique is costly and requires a series of process steps.

3.4.2 Solder bump fabrication by plasma-induced dewetting of Sn film

With the dewetting results on smooth substrates, an attempt was made to produce an array of Sn particles of similar size using template C to imitate the Sn solder bumps used in semiconductor packaging. The leveled floors in the trenches were made intentionally to simulate metal pads on the semiconductor chips (Figure 3-4-3a). After depositing a specific amount of Sn film on the templated substrate to form one particle per trench, hydrogen plasma treatment was conducted at different RF powers. Overall, most particles formed inside the trench areas in contact with the trench floors as shown in the cross-sectional view of Figure 3-4-3b. After dewetting at 300 W, only an approximated 75 percent of the trenches were filled

with Sn particles of considerably different sizes (Figure 3-4-3c). With the RF power increased from 300 W to 800 W, particles of similar size were observed without any empty trenches (Figure 3-4-3b).

A dewetting experiment with a template substrate was also conducted by thermal annealing deposited Au films in a nanometer scale, and the dewetted results were explained by Au film thickness and template geometry [21]. It has been described that a mass flux of the surface film from the positive curvature to the negative curvature causes the film to flatten, and holes occur at the top of the trench walls when the top surface film meets the substrate surface. In this experiment, however, the dewetting behavior was dependent on the RF power. Unlike the case of thin Au films, holes were formed on the surface of the trench sidewalls rather than at the top of the sidewalls (Figure 3-4-3d). The dewetting mechanism on the trench patterns of micrometer scale Sn film may differ from that of the nanometer scale Au film. During plasma treatments of high RF power, large numbers of holes nucleate, separating and distributing the Sn film evenly into the trench areas producing particles of similar size. At lower RF power conditions, the film fails to separate evenly due to insufficient hole nucleation, producing islands that spread across neighboring trenches, agglomerate into particles of varying size, and leave empty trenches.

The findings obtained from the high RF power dewetting results on template C suggested a new design for the fabrication of solder bumps (Figure 3-4-4). In this design, the number of photolithography steps decreased to one, allowing reduction in manufacturing cost and time. Figure 3-4-5 shows the SEM images of the last three steps of this new process.

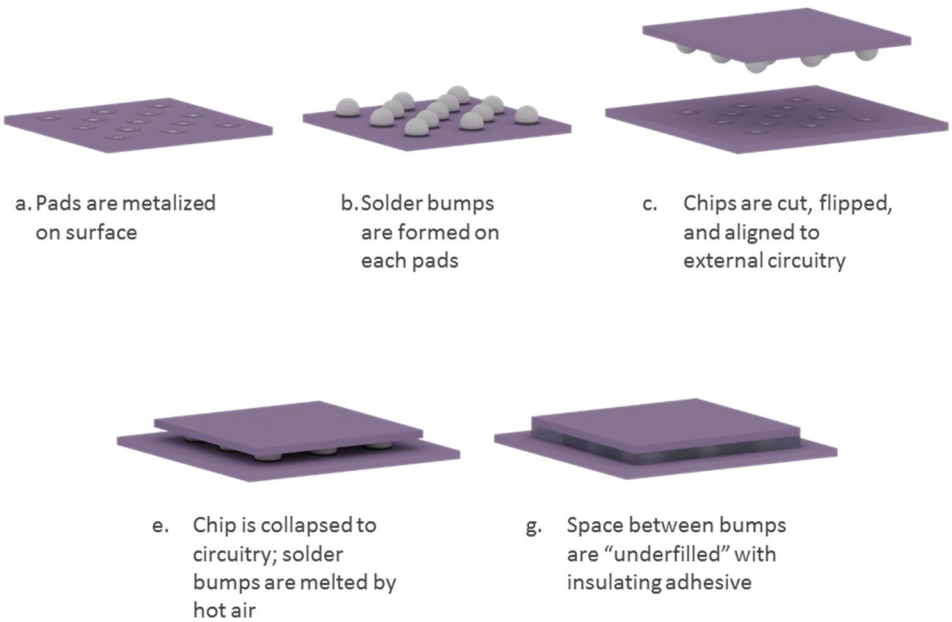

Figure 3-4-1. Illustration of semiconductor chip connecting to external circuitry via solder bumps.

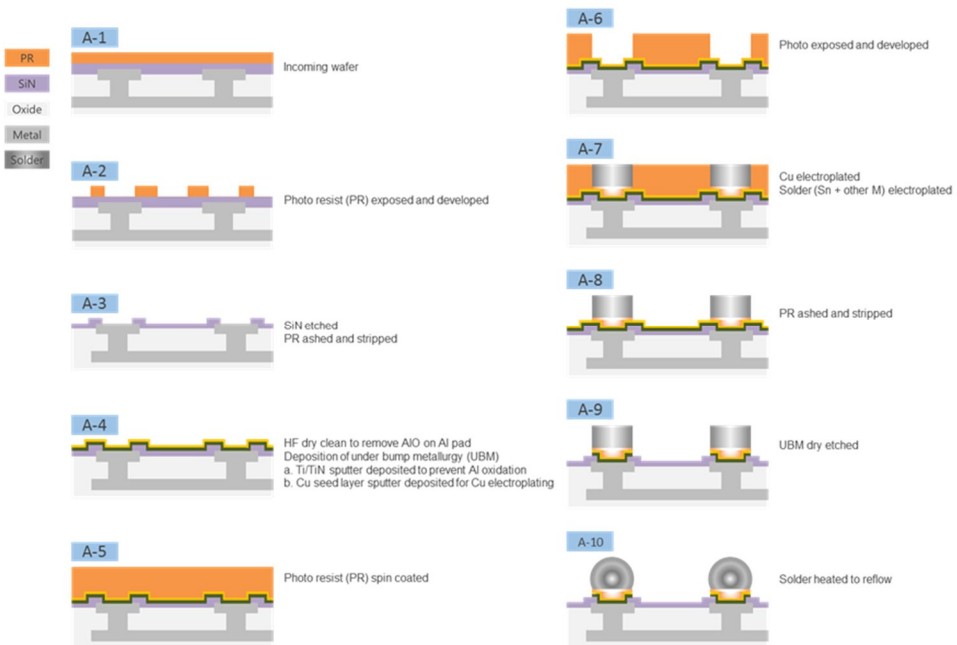

Figure 3-4-2. Illustration of conventional solder bump process.

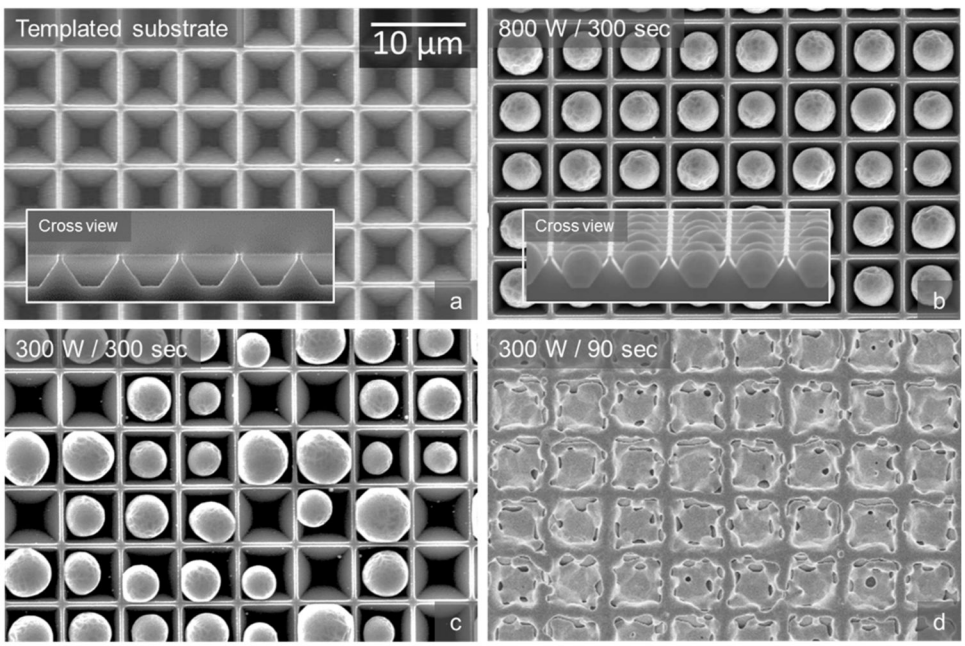

Figure 3-4-3. SEM images of H_2 plasma dewetting of 1600 nm Sn film on template C. Input RF power and plasma treatment time are indicated in each image.

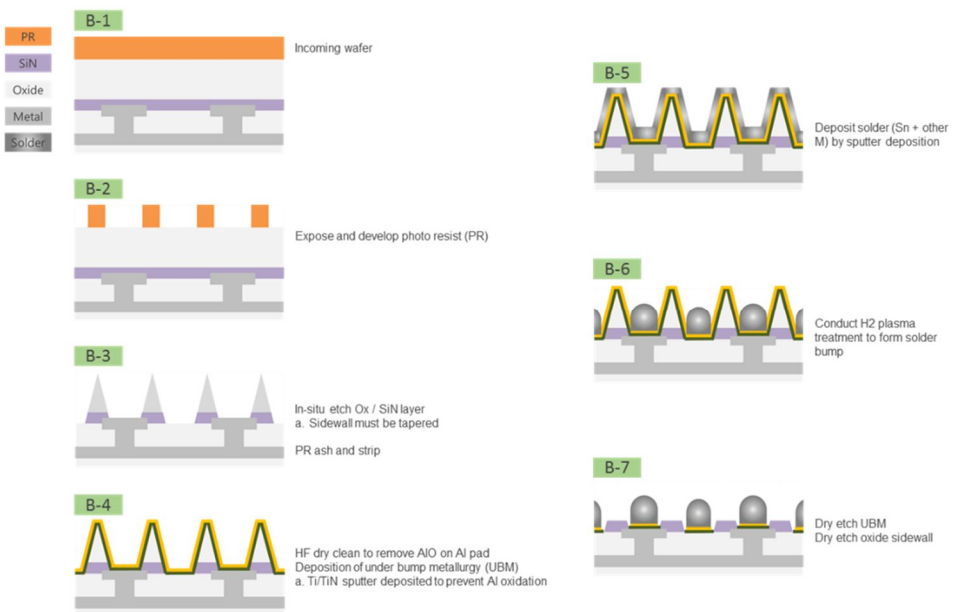

Figure 3-4-4. Illustration of solder bump process by plasma-induced dewetting.

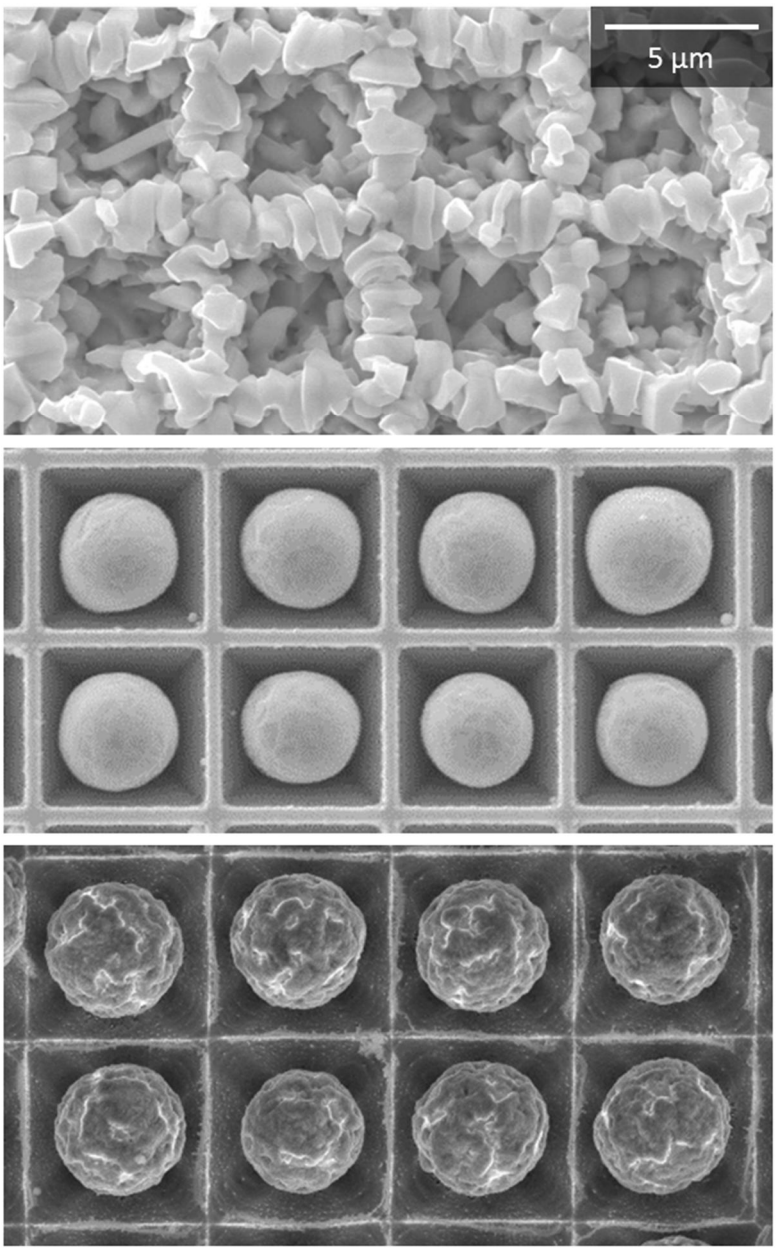

Figure 3-4-5. SEM images of last three steps of solder bump process by plasma induced-dewetting.

3.5 Application II: Sn film dewetting for metal mesh transparent conductive film fabrication

3.5.1 Introduction of metal-based transparent conductive films

The market for transparent conductive films (TCFs) is expected to reach US $ 1.2 billion in 2025 [22]. The dominant portion of this market will still be indium tin oxide (ITO). However, forecasts predict that, due to the physical limitations of ITO on flexible applications and shortage of indium supply, considerable amount of the market will be shared with ITO alternatives. Much research is conducted on fabricating metal based TCFs [23-28]. Metal films intrinsically possess high conductivity due to their free electron density, and their optical, electrical, and physical properties have been demonstrated in many ways to be promising not only for flat touch screens, but also flexible and foldable applications. Ultimately, the two most important properties of TCFs are optical transparency and conductivity, and they had been the research focus on developing ITO alternatives. However, after validating the performance of metal-based TCFs, the focus is currently shifting towards low cost and mass fabrication methods.

3.5.2 Metal mesh transparent conductive film fabricated by plasma-dewetted Sn particle mask

In this experiment, a simple and cost effective fabrication method for meshed-type metal-based TCFs using plasma dewetted Sn particle mask was investigated. Plasma dewetting enables the synthesis of a well-distributed mask

pattern for the mesh areas of the TCF without implementing the costly multi-step photolithography process. Due to its low melting temperature, the dewetting of Sn film occurs rapidly under a hydrogen-based plasma treatment at room temperature. Depending on the initial thickness of the Sn film, results in section 3.3 have shown that nanometer to micrometer scale particle arrays are produced within a few minutes. Using this technique, metal mesh TCF can be directly fabricated on glass and as well as on polymer substrates.

The fabrication method of the metal mesh TCF in this experiment consists of four steps. First, the substrate material is selected, and Sn film is deposited on the surface substrate (Figure 2-3-1a). The substrate material can be glass or polymer, and the Sn film can be deposited via magnetron sputtering or evaporation. In this experiment, the metal mesh was fabricated on both glass and polycarbonate substrates, and DC magnetron sputtering was conducted to deposit the Sn films. Second, the Sn film is dewetted into an array of particles by hydrogen plasma treatment (Figure 2-3-1b). Third, conductive layer is deposited on the sample surface (Figure 2-3-1c). The feasibility of this fabrication method was tested with DC sputtered Au, but other metals, such as Ag and Cu, are also suitable for the conductive layer. Fourth, Sn particle mask layer is removed by a selective wet etch process using hydrochloric acid (HCl) solution (Figure 2-3-1d). HCl reacts with Sn by the following chemical equation:

$$Sn\ (s) + 2\ HCl\ (aq) \rightarrow SnCl_2\ (aq) + H_2(g) \qquad (1)$$

Glass and PC are resistant to HCl [29]. Au does not react with HCl unless there is an additional oxidizing agent present in the solution. Accordingly, an array

of open areas develop when the Sn particles are removed, leaving a mesh-type Au film on the substrate surface.

Before conducting the experiment on PC substrates, which are easily scratched and sensitive to processing temperatures, preliminary experiments were carried out on glass substrates. Sn films from 33 nm to 100 nm were deposited and plasma dewetted to synthesize particles of different size distribution. Figure 3-5-1 shows the plan-view SEM images of the Au mesh electrodes after removing the Sn particles. As shown in the images, each Sn film thickness produces a different particle size distribution and yields mesh patterns of different open area percentage. The open area percentages of the mesh electrodes were measured using a computer software and plotted as a function of Sn film thickness along with the average transmittance of the samples from wavelength 400 nm to 700 nm (Figure 3-5-2). From this plot, it can be seen that the transmittance values follow the trend of the open area percentage. Both transmittance and open area show maximum values at Sn 50 nm and decrease with Sn film thickness. Also, considering the transmittance values measured for the as-deposited Au films, the experimental transmittance results are fairly consistent with the expected values, which are calculated by the open area percentage and the transmittance of the as-deposited Au films. These observations verify that the fabrication method using the Sn particles is effective in producing well-defined mesh patterns, and the mesh patterns are tunable by the distribution of the Sn particles.

The sheet resistance of the samples were collected and plotted as a function of Au film thickness (Figure 3-5-3). The total range of the sheet resistance of the samples varied from 40 to 105 Ω/sq while the thickness of the conductive layer, Au

film, ranged from 8 to 12 nm. Although the conductive film varies very little in thickness, a noticeable trend in sheet resistance is observed. Some of the Au 8 nm resistance values are omitted in the plot because their values were several hundred Ω/sq and could not be plotted on the same scale.

The values of Figure 3-5-2 and 3-5-3 were merged together as shown in Figure 3-5-4 to observe the transmittance of the samples with respect to their sheet resistance. Overall, the tradeoff between optical transmittance and electrical conductivity is apparent. Still, some samples showed comparably higher transmittance, while having lower sheet resistance than others. After comparing the sample results on glass substrates, the sample condition with relatively high transmittance (85 %) and low sheet resistance (77 Ω/sq) was transferred on PC substrate.

For the 50 nm Sn film deposited for the mask layer on the PC substrate, film separation was monitored after only a few seconds of hydrogen plasma treatment. In Figure 3-5-5, the Au mesh films before and after Sn mask removal are shown at different times of hydrogen plasma treatment of the Sn film. During the dewetting process of Sn film, the film morphology gradually changes, resulting in varying amounts of substrate surface area being covered by the Sn film. When the mask is etched away in HCl solution, this covered area is directly converted to open areas in the subsequently deposited Au film. After 7 seconds of plasma treatment, the Sn film is separated into smaller pieces of islands, however, the islands are yet to be fully dewetted and are spread thin on the substrate surface. After longer plasma treatment times, the islands agglomerate into particles, and the area covered by the mask layer decreases. In this experiment, from 10 to 30

seconds of hydrogen plasma treatment of the mask layer, the open area of the Au mesh film decreased from 62 % to 52 %, and the average transmittance varied from 80 to 76 % (Figure 3-5-6).

When comparing the performance of the fabricated Au mesh film on glass and PC substrates, the sheet resistance values were comparable, but a five to nine percent decrease in transmittance was noticed in the PC substrate samples. There are two factors that could have led to the decrease in transmittance. First is the decrease in the open area percentage of the mesh film made on PC substrate. Although the same 50 nm Sn film was deposited and treated with the same hydrogen plasma, lower open area percentages were measured from the mesh films on the PC substrates. The process of metal film dewetting is affected by the surface energies in the metal film to substrate system and the density of holes nucleating at the initial stage of the dewetting process [2]. Accordingly, the change in substrate material from glass to PC inevitably changes both of these variables and produces different size distributions of the Sn particles.

The second factor in decreased transmittance is expected to come from substrate damage during the plasma treatment of the PC substrate. The plasma treatment, conducted to dewet the Sn film, is carried out for less than a minute at room temperature. Thus, there is hardly any effect on the bulk of the PC material. However, while the plasma energy transfers through ion bombardment to the PC surface, some changes occur on the PC substrate surface. The changes in substrate surface were verified by XPS and transmittance measurements using bare PC substrates. The XPS data of bare PC surface after plasma treatment is shown in Figure 3-5-7. To observe the change in binding energies, the O1s peak was

deconvoluted into C-O and C=O peaks by curve fitting. With plasma treatment time, the intensity of C=O decreases while the intensity of C-O increases. Interpretation of this phenomenon is still unclear, but it is certain that changes in the binding energies are occurring on PC surface during the plasma treatment process.

To observe the influence of hydrogen plasma treatment on sample transmittance, bare PC substrates were plasma treated using the same experimental condition. The normalized transmittance of the PC substrates after the plasma treatment is shown in Figure 5a. As shown in the figure, a gradual fall in transmittance is observed from 400 to 600 nm wavelengths. Considering that a similar decrease in transmittance is observed in the Au mesh made on PC substrates (Figure 3-5-8), it is possible that the hydrogen plasma is affecting the PC surface while dewetting the Sn film. Based on these observations, in order to obtain highest transmittance on PC, the plasma treatment of Sn film should be conducted just enough to separate the film into individual islands. This way, there is minimum plasma effect on PC substrate, and the open area percentage is high in the resulting mesh film.

Compared to the fabrication method and performance of other metal-based TCFs, current fabrication method is simple, yet the performance needs much improvement, especially in terms of sheet resistance if it will be used for commercial applications [24]. The decrease in transmittance of PC samples after plasma treatment is another variable that requires attention. Both transmittance and sheet resistance are expected to be enhanced when enlarging the mesh areas in the film. Since the experimental results have verified that the Sn mask pattern, which

directly shapes the mesh areas, is tunable by initial film thickness and plasma dewetting time, testing of a wider range of variables and process optimization is anticipated to yield sufficient improvements in the performance of the Au mesh transparent conductive film.

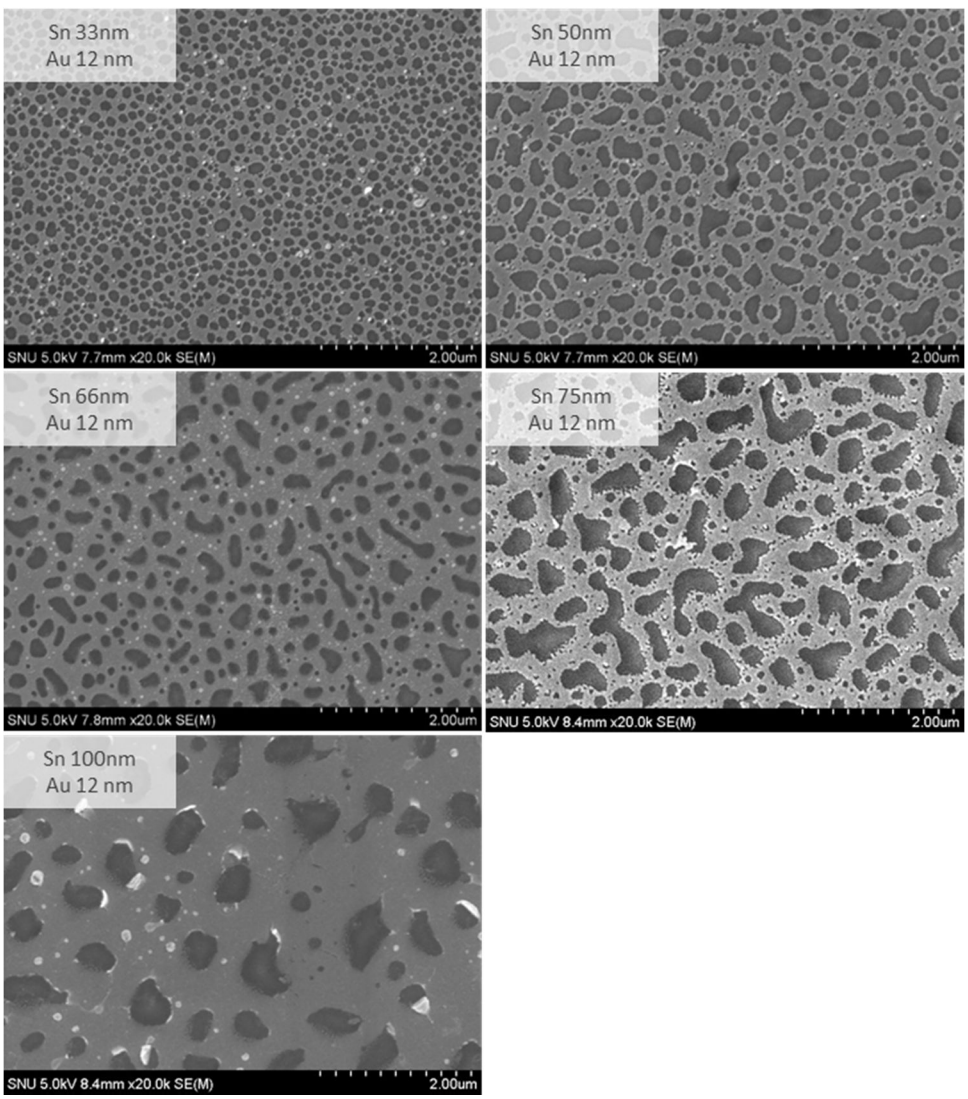

Figure 3-5-1. SEM images of Au mesh film on glass substrate. Initial thickness of Sn film before H_2 plasma treatment and Au film are indicated in each image.

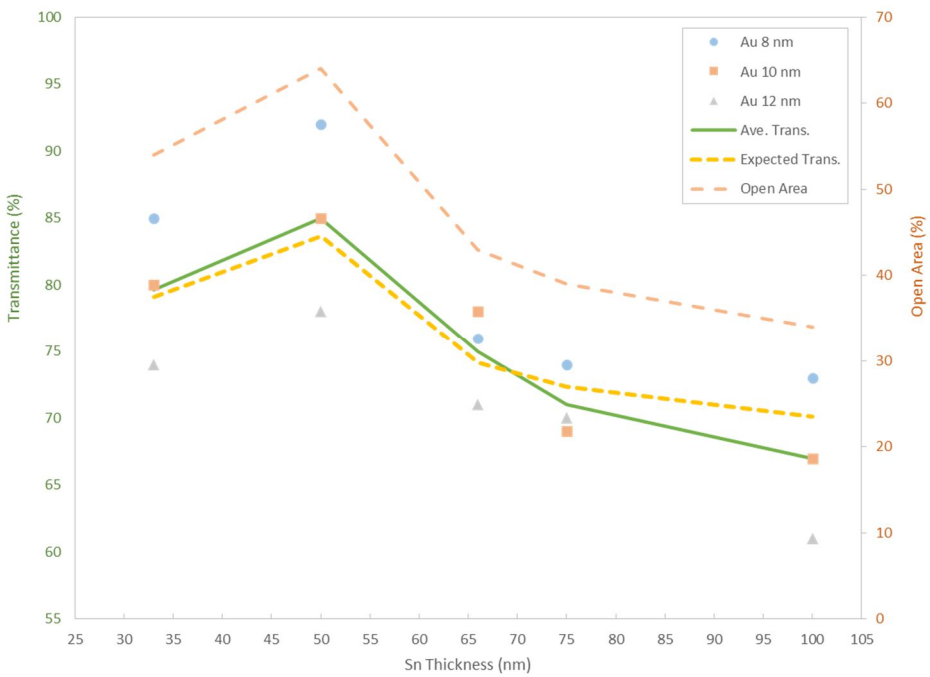

Figure 3-5-2. Transmittance and open area percentage of Au mesh film on glass substrate as a function of initial Sn film thickness. Average transmittance of Au 8, 10, and 12 nm is abbreviated as Ave. Trans. Expected transmittance refers to the calculated average value using the measured open area percentage and the transmittance of the as-deposited Au film of 8, 10, and 12 nm. The transmittance values measured for the as-deposited 8, 10, and 12 nm Au films were 64, 56, and 44 %, respectively.

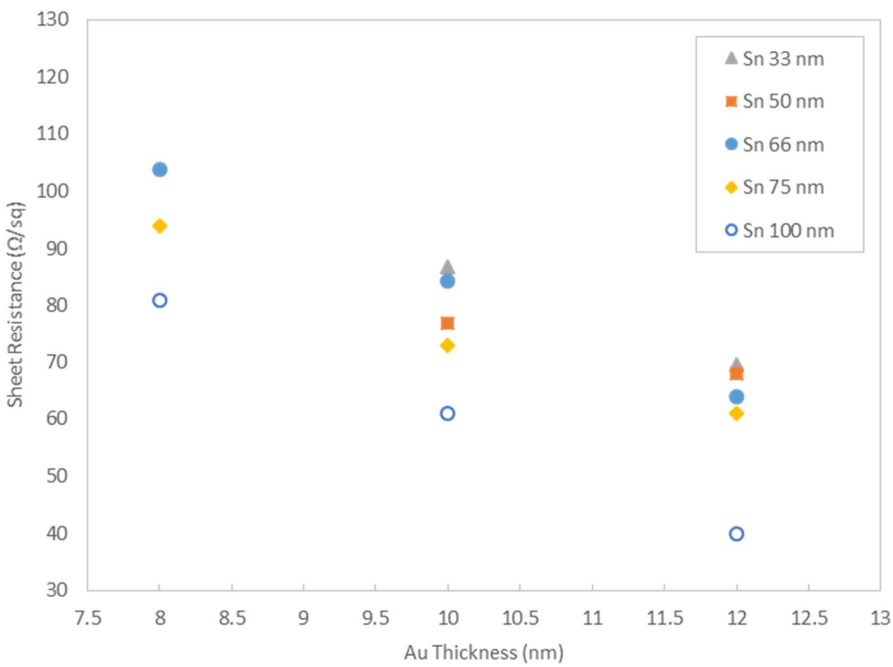

Figure 3-5-3. Sheet resistance of Au mesh film on glass substrate as a function of Au film thickness.

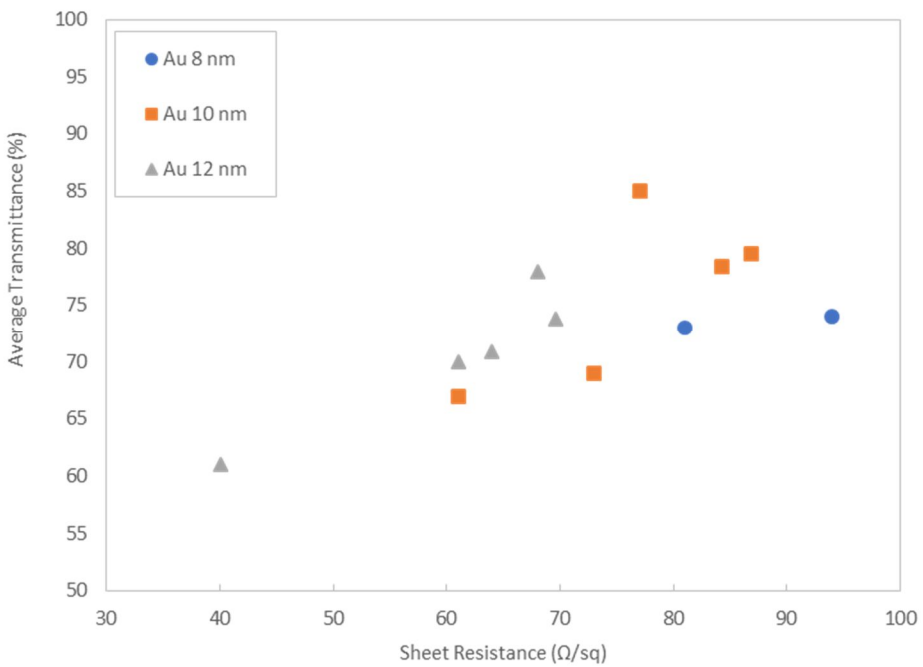

Figure 3-5-4. Transmittance of Au mesh film on glass substrate as a function of sheet resistance.

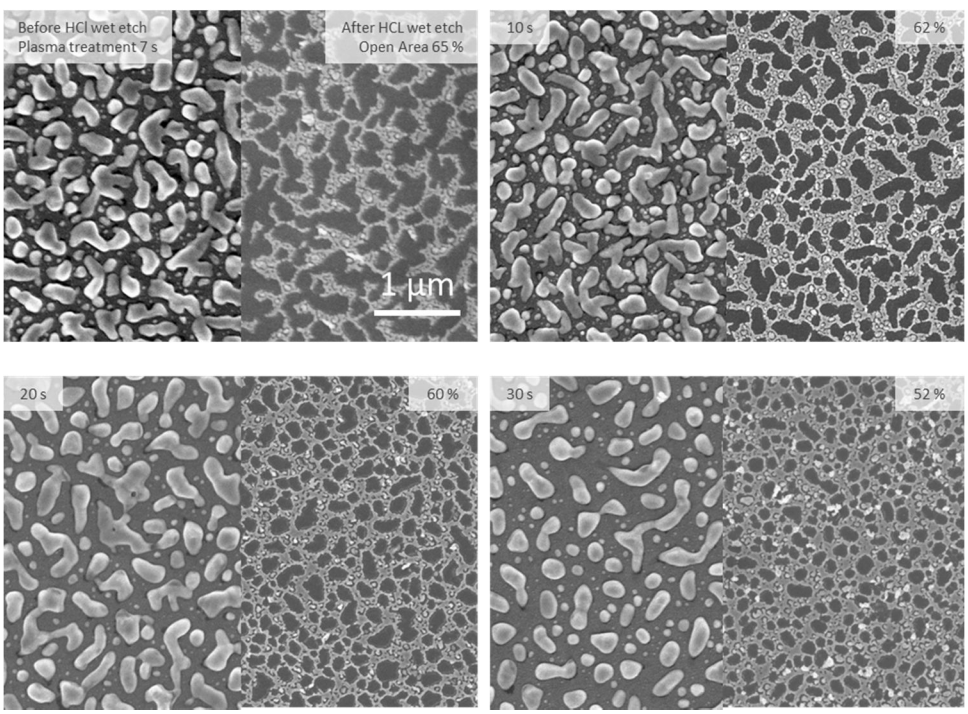

Figure 3-5-5. SEM images of Au mesh film on PC substrates. H_2 plasma treatment time and open area percentage of Au mesh are indicated on top left and right corners of each image.

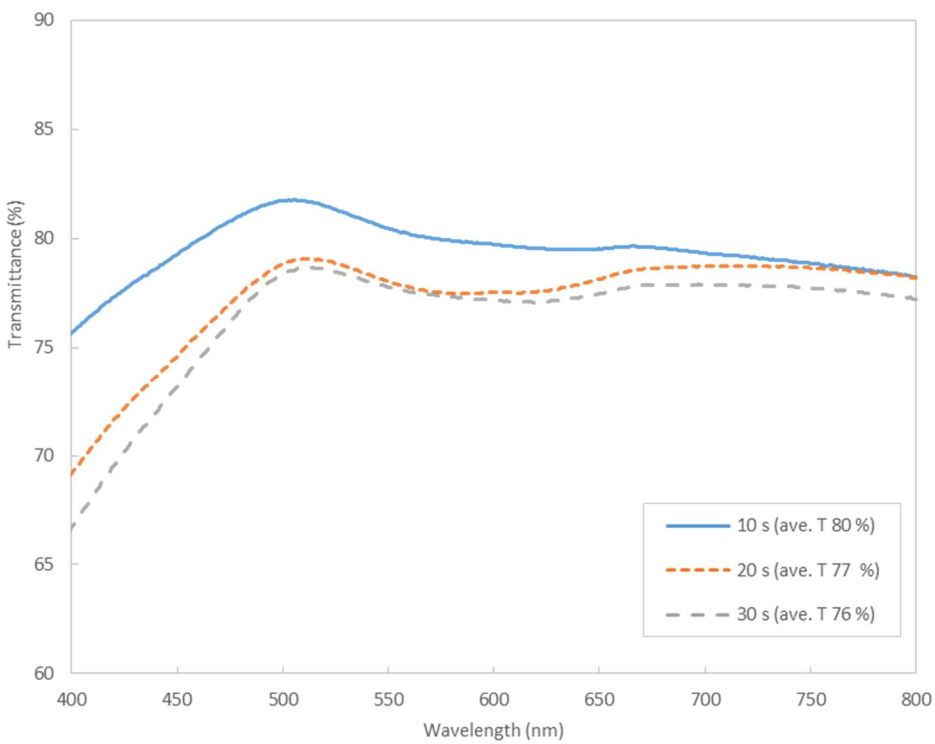

Figure 3-5-6. Transmittance of Au mesh film on PC substrate as a function of wavelength.

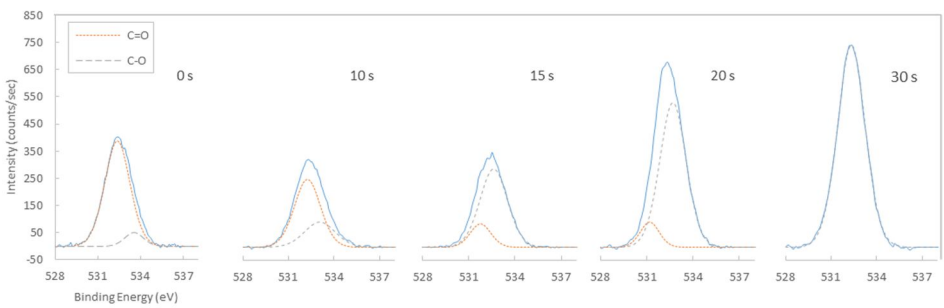

Figure 3-5-7. XPS data of polycarbonate substrate surface after H_2 plasma treatment. Plasma treatment time is indicated in each plot.

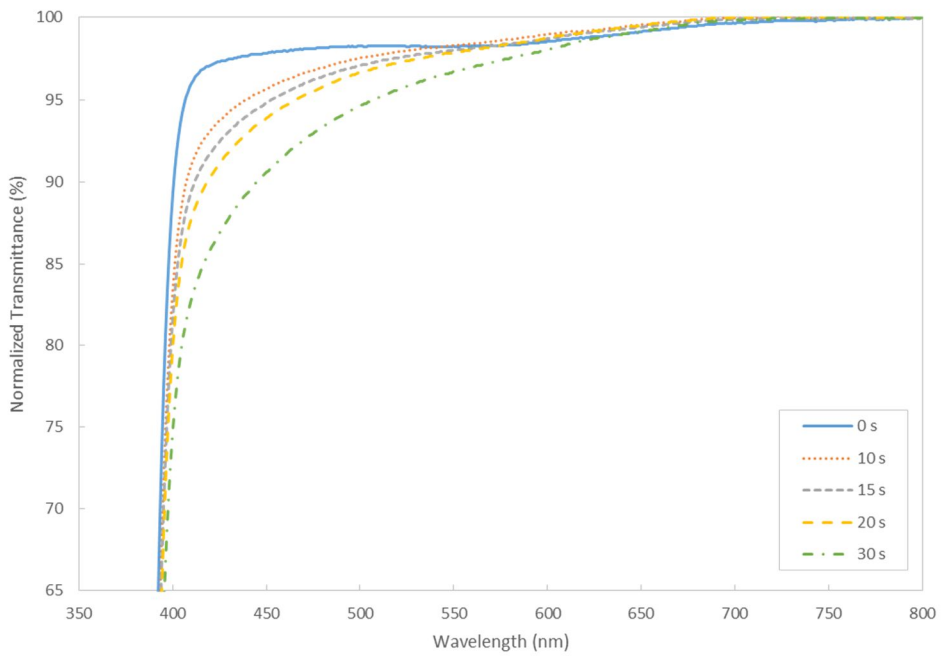

Figure 3-5-8. Normalized transmittance of polycarbonate substrate after H_2 plasma treatment.

IV. Conclusion

The dewetting mechanism of H_2 plasma treated Sn film on smooth substrates was investigated at various film thicknesses. At film thickness < 600 nm, the dewetted particle size showed a spinodal-like dewetting behavior by varying exponentially to the film thickness. At higher film thicknesses, a linear relationship between the particle size and film thickness was observed, which implied that film dewetting was activated by hole nucleation and growth. The morphological evolution of 1600 nm Sn film during the dewetting process and EBSD inspection of the hole nucleation stage confirmed the nucleation and growth mechanism. The different dewetting behaviors were explained by discussing the energy gradient and gravitational force developing in the thicker films.

When varying the RF power during plasma treatment, dewetted particles on smooth substrate showed changes in particle size and size distribution. At film thickness regions of hole nucleation and growth mechanism, test conditions of relatively high RF powers produced smaller particle size along with higher size uniformity compared to results of low RF powers. Likewise, when applying high RF power on Sn films deposited on templated substrates, particles of similar size were produced without any empty trenches. In both smooth and templated substrates, the RF power, which determines the ion density and electron temperature of the plasma, is presumed to affect the hole nucleation rate during Sn film dewetting; raising the RF power increases the number of hole formation and separates the film into reduced areas that subsequently agglomerate into particles of reduced size and reduced size distribution. Repeating the dewetting sequence further expanded the scope of particle distribution attainable by metal film

dewetting. Depending on the relative thicknesses of the first and second films, increasing particle density and producing a bimodal particle distribution was made possible.

A uniformly distributed particle mask layer was produced on PC substrates by implementing a room temperature plasma dewetting process on Sn film. After depositing the Au conductive layer over the dewetted Sn particles and dissolving the Sn particles by HCl, a mesh-type Au transparent conductive film was fabricated. Within the experimental conditions discussed in this work, a sample made on glass substrate showed an optimum performance of 85 % transmittance with 77 Ω/sq.

References

[1] D.T. Danielson, D.K. Sparacin, J. Michel, L.C. Kimerling, Surface-energy-driven dewetting theory of silicon-on-insulator agglomeration, J Appl Phys, 100 (2006).

[2] F. Spaepen, Mechanics and Physics of Layered and Graded MaterialsSubstrate curvature resulting from the capillary forces of a liquid drop, Journal of the Mechanics and Physics of Solids, 44 (1996) 675-681.

[3] A. Vrij, J.T.G. Overbeek, Rupture of thin liquid films due to spontaneous fluctuations in thickness, Journal of the American Chemical Society, 90 (1968) 3074-3078.

[4] F.B. Wyart, J. Daillant, Drying of solids wetted by thin liquid films, Canadian Journal of Physics, 68 (1990) 1084-1088.

[5] G. Reiter, Dewetting of thin polymer films, Phys Rev Lett, 68 (1992) 75-78.

[6] J. Bischof, D. Scherer, S. Herminghaus, P. Leiderer, Dewetting modes of thin metallic films: Nucleation of holes and spinodal dewetting, Phys Rev Lett, 77 (1996) 1536-1539.

[7] D.J. Srolovitz, S.A. Safran, Capillary instabilities in thin films. I. Energetics, J Appl Phys, 60 (1986) 247-254.

[8] K. Sieradzki, K. Bailey, T.L. Alford, Agglomeration and percolation conductivity, Applied Physics Letters, 79 (2001) 3401-3403.

[9] J.Y. Kwon, T.S. Yoon, K.B. Kim, S.H. Min, Comparison of the agglomeration behavior of Au and Cu films sputter deposited on silicon dioxide, J Appl Phys, 93 (2003) 3270-3278.

[10] F. Niekiel, P. Schweizer, S.M. Kraschewski, B. Butz, E. Spiecker, The process of solid-state dewetting of Au thin films studied by in situ scanning transmission electron microscopy, Acta Mater, 90 (2015) 118-132.

[11] H. Krishna, C. Favazza, A.K. Gangopadhyay, R. Kalyanaraman, Functional nanostructures through nanosecond laser dewetting of thin metal films, JOM, 60 (2008) 37-42.

[12] Y. Kojima, T. Kato, Nanoparticle formation in Au thin films by electron-beam-induced dewetting, Nanotechnology, 19 (2008).

[13] S.H. Kwon, D.H. Han, H.J. Choe, J.J. Lee, Synthesis of copper nanoparticles by solid-state plasma-induced dewetting, Nanotechnology, 22 (2011).

[14] M.J. Beliatis, S.J. Henley, S. Han, K. Gandhi, A.A.D.T. Adikaari, E. Stratakis, E. Kymakis, S.R.P. Silva, Organic solar cells with plasmonic layers formed by laser nanofabrication, Physical Chemistry Chemical Physics, 15 (2013) 8237-8244.

[15] J. Li, H. Zhou, S. Qian, Z. Liu, J. Feng, P. Jin, X. Liu, Plasmonic gold nanoparticles modified titania nanotubes for antibacterial application, Applied Physics Letters, 104 (2014) 261110.

[16] B.J.M. Hausmann, M. Khan, Y. Zhang, T.M. Babinec, K. Martinick, M. McCutcheon, P.R. Hemmer, M. Lončar, Fabrication of diamond nanowires for quantum information processing applications, Diamond Relat. Mat., 19 (2010) 621-629.

[17] Y. Wang, V. Schmidt, S. Senz, U. Gosele, Epitaxial growth of silicon nanowires using an aluminium catalyst, Nat Nano, 1 (2006) 186-189.

[18] S.H. Kwon, H.J. Choe, H.C. Lee, C.W. Chung, J.J. Lee, Control of size uniformity of Cu nanoparticle array produced by plasma-induced dewetting, J. Nanosci. Nanotechnol., 15 (2015) 2542-2546.

[19] S.H. Kwon, H.J. Choe, H.C. Lee, C.W. Chung, J.J. Lee, Mechanism of solid-state plasma-induced dewetting for formation of copper and gold nanoparticles, J. Nanosci. Nanotechnol., 13 (2013) 6109-6114.

[20] P.A. Gruber, L. Bélanger, G.P. Brouillette, D.H. Danovitch, J.L. Landreville, D.T. Naugle, V.A. Oberson, D.Y. Shih, C.L. Tessler, M.R. Turgeon, Low-cost wafer bumping, IBM J. Res. Dev., 49 (2005) 621-639.

[21] A.L. Giermann, C.V. Thompson, Requirements for graphoepitaxial alignment through solid-state dewetting of Au films, J Appl Phys, 109 (2011).

[22] K. Ghaffarzadeh, Transparent Conductive Films (TCF) 2015-2025: Forecasts, Markets, Technologies, IDTechEX, 2015.

[23] H. Wu, L. Hu, M.W. Rowell, D. Kong, J.J. Cha, J.R. McDonough, J. Zhu, Y. Yang, M.D. McGehee, Y. Cui, Electrospun metal nanofiber webs as high-performance transparent electrode, Nano Lett., 10 (2010) 4242-4248.

[24] D.S. Hecht, L. Hu, G. Irvin, Emerging transparent electrodes based on thin films of carbon nanotubes, graphene, and metallic nanostructures, Adv Mater, 23 (2011) 1482-1513.

[25] L. Hu, H. Wu, Y. Cui, Metal nanogrids, nanowires, and nanofibers for transparent electrodes, MRS Bulletin, 36 (2011) 760-765.

[26] H. Wu, D. Kong, Z. Ruan, P.C. Hsu, S. Wang, Z. Yu, T.J. Carney, L. Hu, S. Fan, Y. Cui, A transparent electrode based on a metal nanotrough network, Nat. Nanotechnol., 8 (2013) 421-425.

[27] C.F. Guo, T. Sun, Q. Liu, Z. Suo, Z. Ren, Highly stretchable and transparent nanomesh electrodes made by grain boundary lithography, Nat. Commun., 5 (2014).

[28] E.J. Lee, Y.H. Kim, D.K. Hwang, W.K. Choi, J.Y. Kim, Synthesis and optoelectronic characteristics of 20 nm diameter silver nanowires for highly transparent electrode films, RSC Adv., 6 (2016) 11702-11710.

[29] Chemical Compatibility Guide, Thermo Fisher Scientific.

국문초록

비정질 기판에 PVD 로 증착된 금속 박막은 에너지적으로 준안정 상태이다. 이 기판에 충분한 에너지가 전달 되었을 때, 시스템의 에너지를 줄이기 위하여 박막의 원자들은 확산을 통해 분말의 형태로 디웨팅 된다. 금속 박막 디웨팅은 홀 생성부터 시작을 한다. 홀 생성의 방식은 크게 두 가지로 스피노달 디웨팅 또는 hole nucleation and growth 가 있다. 홀 생성의 방식에 따라 분말의 크기 및 분포도의 결과가 다르다.

본 연구에서는 Sn 박막의 디웨팅을 연구하였다. 50 에서 2000 nm 두께의 Sn 박막을 수소 플라즈마로 디웨팅하는 과정에서 스피노달 디웨팅과 hole nucleation and growth 의 특징을 모두 볼 수 있었다. 두께가 얇은 공정 조건에서는 분말의 크기가 박막 두께에 따라 기하급수적으로 성장하는 스피노달 디웨팅의 특징을 확인하였다. 반면, 상대적으로 두꺼운 박막 조건에서는 분말의 성장이 박막 두께에 비례하여 hole nucleation and growth 방식으로 디웨팅이 활성화되었다.

Sn 분말의 크기와 분포도를 조절하기 위하여 다양한 조건을 시도하였다. 플라즈마에 인가되는 RF power 는 플라즈마의 밀도와 전자 온도에 영향을 준다. 이 RF power 를 증가 하였을 때, 동일한 박막 두께의 조건에서 다양한 분말 크기와 분포도 결과를 얻을 수 있었다.

Repeated 디웨팅과 트렌치 패턴 기판을 접목 시켰을 때, 더욱 다양한 박막 디웨팅의 결과를 얻을 수 있었다.

Sn 박막 디웨팅의 연구 결과를 두 가지 산업 기술에 응용 하였다. 첫 번째는 반도체 패키징에서 사용되는 솔더 범프의 응용이다. 반도체 공정으로 완성된 IC 칩은 솔더 범프 또는 솔더 조인트를 이용하여 외부회로와 연결된다. 현재의 솔더 범프 과정은 두 차례의 포토리소그라피 공정을 필요로 하고 있다. 본 연구에서는 이 솔더 범프 만드는 과정을 박막 디웨팅의 self-assemble 특성을 사용하여 간소화 시켰다.

Sn 박막 디웨팅의 두 번째 응용으로는 메쉬 형태의 금속 투명 전도막을 만들었다. 플라즈마 공정의 저온 특성을 이용하여 폴리머 기판 위에 직접 Sn 분말을 생성하였고, Au 의 전도막 증착 후 선택적으로 Sn 을 제거하여 메쉬 형태의 전도막을 완성 시켰다. Sn 분말의 분포도를 조절하여 메쉬 영역에 변화를 주었고, 이 변화에 따라 넓은 범위의 투명도와 전기 저항 값을 갖는 투명 전도막을 만들 수 있었다.

Sn 박막과 금속 전도막의 증착은 DC 마그네트론 스퍼터를 이용하였고, Sn 박막의 플라즈마 처리는 ICP 를 장착한 진공챔버에서 진행을 하였다. 디웨팅된 분말과 투명 전도막의 표면은 FESEM 으로 관측을 하였고, SEM 사진을 컴퓨터 프로그램을 이용하여 통계적인 데이터를 얻을 수 있었다.

주요어: 디웨팅, 플라즈마, 주석, 분말, 솔더범프, 투명전도막,

유도결합플라즈마

학번: 2010-23199